Journal of Nuclear Medicine, published on December 8, 2022 as doi:10.2967/jnumed.122.264494

# Fibroblast activation protein targeted radioligand therapy for treatment of solid tumors

Spencer D. Lindeman,[1*] Ramesh Mukkamala,[1] Autumn Horner,[1] Pooja Tudi,[1] Owen C. Booth,[1] Roxanne Huff,[1] Joshua Hinsey,[1] Anders Hovstadius,[1] Peter Martone,[1] Fenghua Zhang,[1] Madduri Srinivasarao,[1] Abigail Cox,[2] Philip S. Low[1†]

[1]Department of Chemistry and Institute for Drug Discovery, Purdue University; West Lafayette, Indiana 47907, United States

[2]Department of Comparative Pathobiology, Purdue College of Veterinary Medicine; West Lafayette, Indiana 47907, United States

**Disclaimer:** Spencer D. Lindeman, Ramesh Mukkamala, Madduri Srinivasarao, and Philip S. Low hold a patent on FAP-targeted radioligand therapy. Other authors declare no potential conflicts of interest.

**†Corresponding author:** Philip S. Low | 720 Clinic Drive, West Lafayette, IN 47907 | Phone: 765-494-5283 | Fax: 765-494-5272 | plow@purdue.edu

***First author:** Spencer D. Lindeman, post-doctoral fellow | 720 Clinic Drive, West Lafayette, IN 47907 | Phone: 765-494-1654 | Fax: 765-494-5272 | lindemas@purdue.edu

**Word count:** 4976

**Financial support:** Purdue Professorship

**Running title:** FAP-targeted radioligand therapy

**ABSTRACT**

**Background:** Fibroblast activation protein (FAP) has received increasing attention as an oncological target because of its prominent expression in solid tumors but virtual absence from healthy tissues. Most radioligand therapies (RLT) targeting FAP, however, suffer from inadequate tumor retention or clearance from healthy tissues. Herein we report a FAP-targeted RLT comprised of a FAP6 ligand conjugated to DOTA and an albumin-binder (4-p-iodophenylbutyric acid, IP) for enhanced pharmacokinetics. We evaluated the performance of the resulting FAP6-IP-DOTA conjugate in four tumor models, three of which expressed FAP only on cancer-associated fibroblasts (CAFs) i.e., analogous to human tumors.

**Methods:** Single-cell RNA-seq data were analyzed from 34 human breast, ovarian, colorectal, and lung cancers to quantify FAP-overexpressing cells. FAP6-DOTA conjugates were synthesized with or without an albumin-binder (IP) and investigated for binding to human FAP-expressing cells. Accumulation of $^{111}$In- or $^{177}$Lu-labeled conjugates in KB, HT29, U87MG, and 4T1 murine tumors were also assessed by radioimaging and/or biodistribution analyses. Radiotherapeutic potency was quantitated by measuring tumor volumes versus time.

**Results:** Approximately 5% of all cells in human tumors overexpressed FAP (CAFs comprised ~77% of this FAP-positive subpopulation, while ~2% were cancer cells). FAP6 conjugates bound to FAP-expressing cells with high affinity ($K_d$ ~1 nM). $^{177}$Lu-FAP6-IP-DOTA achieved 88-fold higher tumor dose than $^{177}$Lu-FAP6-DOTA and improved all tumor-to-healthy organ ratios. Single doses of $^{177}$Lu-FAP6-IP-DOTA suppressed tumor growth by ~45% in all tested tumor models without causing reproducible toxicities.

**Conclusion:** We conclude that $^{177}$Lu-FAP6-IP-DOTA constitutes a promising candidate for FAP-targeted RLT of solid tumors.

**Keywords:** Radioligand therapy | FAP | albumin-binder | scRNA-seq| cancer-associated fibroblasts

## INTRODUCTION

A subset of cancer-associated fibroblasts (CAFs) are characterized by expression of a cell-surface serine protease termed fibroblast activation protein (FAP) that participates in remodeling of the extracellular matrix during tumor growth and metastasis **(*1*)**. Approximately 90% of epithelial cancers upregulate FAP **(*2*)**, and FAP-targeted PET tracers have been shown to image at least 28 different cancer types in humans **(*3*)**. Due to FAP's broad expression on CAFs and its nearly complete absence from healthy tissues, FAP has recently been explored as a receptor for targeted radioligand therapy (RLT) of a diversity of solid tumors **(*4,5*)**.

Optimal FAP-targeted radiotherapy might be expected to satisfy several criteria. First, it will contain a therapeutic radionuclide that effectively irradiates multiple cancer cells within the vicinity of each CAF. Second, the targeting ligand will possess high affinity and specificity for FAP to minimize uptake by its homologs in healthy organs. Third, the pharmacokinetic properties of the resulting conjugate will be optimized to ensure prolonged tumor accumulation and rapid clearance from normal tissues.

To achieve these objectives, we first derivatized a new FAP targeting ligand (FAP6) with DOTA via a PEG spacer. We then incorporated the established albumin-binder 4-*p*-iodophenylbutyric acid (IP) **(*6*)** into our FAP-targeting radioligand **(Fig. 1)**, since such appendages have been observed to prolong the pharmacokinetics and improve tumor uptake of RLTs **(*7-10*)**. We demonstrate here that the resulting conjugate, FAP6-IP-DOTA, exhibits high FAP affinity, prolonged circulation, increased tumor uptake, and minimal retention in healthy tissues. Moreover, the final $^{177}$Lu-labeled RLT causes no obvious toxicity to healthy tissues while achieving significant anticancer efficacy in four different murine tumor models.

## MATERIALS AND METHODS

Reagents, vendors, syntheses, and full experimental procedures are detailed in the Supplemental Data.

### scRNA-seq Analysis

We analyzed single-cell RNA-sequencing data collected on fresh human tumor samples reported elsewhere **(*11*)**. FAP gene expression was extracted, quantitated, and plotted on a log(2) scale for comparison among different cell types in each cancer tissue, according to online tutorials **(*12*)**.

### Cell Culture and Transduction

4T1, KB, HT29, and U87MG cells were purchased from ATCC and cultured as reported previously **(*13,14*)**. HEK-293T cells with high levels of FAP expression (HEK-hFAP) were generated as formerly described **(*13*)**.

### Radiolabeling

FAP6 conjugates were diluted in ammonium acetate (0.5 M, pH 8.0). $^{111}In$ [$InCl_3$] (Cardinal Health, Indianapolis, IN) was added to obtain a specific activity of ≤4.0 MBq/nmol, or $^{177}Lu$ [$LuCl_3$] (RadioMedix, Houston, TX) ≤11.0 MBq/nmol. The resulting solutions were heated to 90ºC for 10–20 minutes and the radiopurities of the products were analyzed by radio-HPLC. Radiopurity exceeded 95% in all studies.

### Cell Binding Studies

*Flow Cytometry.* Anti-human FAP antibody conjugated to APC dye was used for staining all cell lines except 4T1 cells, which were stained with anti-mouse FAP antibody and then a secondary APC-conjugated antibody.

*Displacement Assay*. HEK-hFAP cells grown to confluency in 24-well plates were co-incubated with FAP6-rhodamine and increasing concentrations of FAP6-DOTA or FAP6-IP-DOTA. Cells were then washed, dissolved, and analyzed by fluorescent plate-reader.

*Binding Assay*. Hs894 CAFs grown to confluency in 24-well plates were incubated with increasing concentrations of $^{111}$In-FAP6-DOTA or $^{111}$In-FAP6-IP-DOTA in the absence or presence of excess FAP6 ligand. Cells were then washed, dissolved, and analyzed by gamma counter.

**Animal Husbandry**

Mice were provided normal rodent chow and water *ad libitum* and maintained on a standard 12-hour light-dark cycle. All animal procedures were approved by the Purdue Animal Care and Use Committee.

**Tumor Models**

Balb/c mice were inoculated on their shoulder with 1 x $10^5$ cells of 4T1 cells. Nu/nu mice were inoculated on their shoulder with 5 x $10^6$ cells of HT29, KB, or U87MG cells.

**SPECT/CT scans**

Tumor-bearing mice were intravenously injected with FAP6 conjugate radiolabeled with ~13 MBq of indium-111. At indicated times, mice were anesthetized, then scanned using an MILabs VECTor/CT instrument. CT scans were reconstructed using NRecon software. The datasets were fused, filtered, and processed using PMOD software (version 3.2).

**Radioactive Biodistribution**

Tumor-bearing mice (n=3–5) were intravenously injected with $^{177}$Lu-FAP6-DOTA or $^{177}$Lu-FAP6-IP-DOTA. At indicated times, mice were euthanized, and organs of interest were harvested, weighed, then analyzed by gamma counter.

**Radiotherapy**

4T1, HT29, KB, and U87MG tumor-bearing mice were randomly divided into control and treatment groups to ensure equal starting tumor volumes. Each cohort received a single intravenous injection of vehicle alone or with $^{177}$Lu-radiolabeled FAP6 conjugate on day 0. Tumors were measured with a caliper in two perpendicular directions every other day. Mice were euthanized upon reaching one of the predefined endpoint criteria according to IACUC regulations.

**Toxicology**

Mice were weighed every other day during radiotherapy as a gross evaluation of health. Tissue sections from organs of interest (n=1–8 per organ per mouse) were preserved and examined blindly for lesions by a board-certified veterinary pathologist.

**Statistical Analysis**

Data were analyzed using GraphPad Prism 8 unless otherwise stated. All results are presented as mean ± SE.

## RESULTS

### scRNA-seq Analysis of FAP Gene Expression in Multiple Human Tumor Types

To better understand how FAP might serve as a target for RLT, we first sought to quantify cells in human tumors that upregulate FAP expression. For this purpose, FAP gene expression data **(Fig. 2)** was extracted from a curated database containing single-cell RNA sequencing (scRNA-seq) analyses of tumors from 14 breast, 5 ovarian, 7 colorectal, and 8 lung cancer patients **(*11*)**. Quantification of the scRNA-seq data **(Supplemental Fig. 1)** revealed that ~30% of all CAFs overexpress FAP RNA. Although ~10% of endothelial cells also overexpressed FAP RNA, only ~2% of cancer cells and <1% of all other cell types upregulated FAP gene expression. Moreover, ~77% of all FAP-overexpressing cells in the average tumor were fibroblasts, suggesting that animal models used for evaluation of FAP-targeted RLTs should derive their FAP-positive cell population primarily from CAFs. And because FAP-overexpressing cells constituted ≤10% of all cells in the average cancer mass (mean=5%), a radionuclide with a large killing radius (e.g., $^{177}$Lu) was deemed prudent for effective FAP-targeted radiotherapy. The variability of FAP expression among different human tumor types further suggested that adjusted doses of radioactivity might be necessary to achieve effective therapeutic responses in different patients.

### Binding of FAP6 Conjugates to Different Cell Lines

Because FAP was not overexpressed on most human cancer cells, we selected cancer cell lines that did not directly express FAP to more accurately mimic FAP expression in human

tumors. As documented in **Fig. 3A**, flow cytometry analyses of 4T1, KB, and HT29 cells using species-specific anti-FAP antibodies demonstrated no FAP expression, even though the same cancers are shown to be FAP-positive in murine tumor models **(Supplemental Fig. 2)** due to infiltration of CAFs **(*13-17*)**. In contrast, fibroblast cell lines Hs894 and WI38, as well as the glioblastoma cell line U87MG, displayed similarly low levels of endogenous FAP expression. HEK293 cells that do not naturally express FAP were transduced to express artificially high levels of human FAP for use as a positive control.

To develop a FAP ligand that could mediate protracted retention of FAP-targeted RLTs in solid tumors, we identified a FAP inhibitor comprising a different scaffold than the quinoline-based ligands most used to date **(*17-23*)**. The FAP6 ligand contains a pyroglutamic-isoindoline–based moiety **(*13,24*)**, which is reported to possess higher selectivity for FAP over PREP (a ubiquitously-expressed homolog) **(*24*)** and longer retention in tumors when conjugated to a near-infrared dye **(*13,25*)**. We then linked FAP6 with DOTA via a PEG-spacer to yield the FAP6-DOTA conjugate **(Supplemental Scheme 1)**. To evaluate the merit of attaching an albumin-binder to FAP6-DOTA, an iodophenyl butyric acid (IP) moiety was inserted to generate FAP6-IP-DOTA **(Supplemental Scheme 2)**. The final structures of FAP6-DOTA **(Fig. 3B)** and FAP6-IP-DOTA **(Fig. 3C)** were characterized by LC/MS **(Supplemental Fig. 3)**. Radiolabeling with indium-111 and lutetium-177 was evaluated by radio-HPLC **(Supplemental Fig. 4)**.

To obtain an initial estimate of the affinity of the FAP6 ligand for FAP, competitive displacement and direct binding curves were generated with both conjugates **(Fig. 3B–C)** in HEK-hFAP and Hs894 CAFs, respectively. FAP6-DOTA and FAP6-IP-DOTA exhibited affinities of ~1 nM for FAP in both cell lines, suggesting that appending the albumin-binder did not significantly affect conjugate affinity. Binding was competitively suppressed by co-incubation with 100x excess FAP6 ligand, confirming that targeting of FAP6 conjugates to FAP-positive cells was receptor-

mediated. Both FAP6 conjugates were also found to internalize into FAP-positive cells **(Supplemental Fig. 5)**, mirroring FAP6-dye conjugates **(*13*)**.

**Tumor Accumulation and Biodistribution of FAP6 Radioligands**

To determine whether insertion of the albumin-binder improves accumulation of FAP6 conjugates in solid tumors, we next compared the biodistributions of both radioligands in tumor-bearing mice wherein the primary FAP-positive cells were CAFs. Balb/c mice inoculated with FAP-negative 4T1 cancer cells were intravenously injected with either $^{111}$In-FAP6-DOTA or $^{111}$In-FAP6-IP-DOTA for radioimaging (see **Supplemental Figs. 6–7** for studies to optimize mass doses). The SPECT/CT scans demonstrated high uptake of $^{111}$In-FAP6-DOTA in the liver but negligible accumulation in the tumors at 2- and 4-hours post-injection **(Fig. 4A)**, presumably due to rapid excretion of $^{111}$In-FAP6-DOTA before its perfusion into poorly vascularized 4T1 tumors. In contrast, radioimages of mice injected with the same dose of $^{111}$In-FAP6-IP-DOTA showed prominent uptake in tumors that persisted for at least 120 hours post-injection (**Fig. 4B**). Additional SPECT/CT scans of HT29, KB, and U87MG tumors demonstrated the versatility of $^{111}$In-FAP6-IP-DOTA tumor targeting and retention (**Supplemental Figs. 7–8**). Competition and untargeted radioimages confirmed that *in vivo* tumor uptake was FAP-mediated (**Supplemental Fig. 9**). Although transient retention was also observed in the kidneys, the absence of significant accumulation in the liver suggested that FAP6-IP-DOTA might constitute an RLT worthy of further scrutiny.

To confirm these results, we next quantitated the biodistributions of each FAP6 conjugate in separate cohorts of 4T1 tumor-bearing mice over time. $^{177}$Lu-FAP6-DOTA demonstrated prolonged accumulation in spleen and liver yet rapid excretion from bloodstream and tumors (**Fig. 4A**), whereas $^{177}$Lu-FAP6-IP-DOTA readily cleared from healthy organs despite its protracted retention in blood and tumors (**Fig. 4B**). The data thus confirm that insertion of an iodophenyl albumin-binder facilitates FAP6 circulation in the bloodstream, thereby avoiding premature capture by excretory organs, which enables increased FAP6 uptake by the CAFs and ultimately saturates the tumor. Dosimetry estimates (**Supplemental Fig. 10**), $^{177}$Lu-FAP6-IP-DOTA SPECT/CT scans,

and $^{111}$In-FAP6-IP-DOTA biodistribution studies were also performed (**Supplemental Fig. 11; Supplemental Table 1**).

**Effect of Albumin-binder on Radiotherapeutic Potencies of FAP6 RLTs**

Encouraged by the improved tumor accumulation conferred by insertion of an albumin-binder, we next compared the radiotherapeutic potencies of the two FAP-targeted RLTs. Moreover, to expand the diversity of tumor types in which the FAP-targeted RLTs would be compared, we employed a human cancer xenograft model (KB cells) reported to respond to radiotherapy **(*7*)**, and in which the only cells overexpressing FAP were again CAFs **(*13,14*)**. Mice bearing tumors generated from FAP-negative KB cells were injected intravenously with a single dose of vehicle alone, or with $^{177}$Lu-FAP6-DOTA or $^{177}$Lu-FAP6-IP-DOTA on day 0. Tumor sizes and body weights were then measured every other day for ten weeks.

Consistent with the above SPECT/CT and biodistribution results, $^{177}$Lu-FAP6-DOTA provided no therapeutic benefit, suppressing tumor growth by only 3% and conferring no prolongation on overall survival (**Fig. 5A**). In contrast, $^{177}$Lu-FAP6-IP-DOTA radiotherapy suppressed tumor growth by ~36% and improved overall survival by an average of ~3 weeks (**Fig. 5B**, p=n.s.). While mice treated with $^{177}$Lu-FAP6-IP-DOTA experienced minor weight loss immediately following injection, the same mice quickly recovered and displayed no persisting toxicities, which also is consistent with the clearance of $^{177}$Lu-FAP6-IP-DOTA from healthy tissues.

**Evaluation of $^{177}$Lu-FAP6-IP-DOTA Treatment in Multiple Tumor Types**

Satisfied that $^{177}$Lu-FAP6-IP-DOTA constituted the better FAP-targeted RLT, we next investigated whether $^{177}$Lu-FAP6-IP-DOTA might effectively treat a diversity of solid tumors, as frequently envisioned by others **(*3,18*)**. Mice bearing HT29, U87MG, or 4T1 tumors were injected intravenously with a single dose of either vehicle alone or with $^{177}$Lu-FAP6-IP-DOTA on day 0, after which tumor sizes and body weights were measured every other day. Growth of HT29 tumors was suppressed ~58% by 9 MBq of $^{177}$Lu-FAP6-IP-DOTA (**Fig. 6A**), but surprisingly this dose did not

affect U87MG or 4T1 tumors (**Supplemental Fig. 12A-B**). To determine whether U87MG or 4T1 tumors might respond to a higher dose of $^{177}$Lu-FAP6-IP-DOTA, additional cohorts of 5 mice per group were injected with 18 MBq of $^{177}$Lu-FAP6-IP-DOTA and monitored. Growth of U87MG tumors was reduced ~41% (**Fig. 6B**), but 4T1 tumors again continued to grow unabated (**Supplemental Fig. 12B**). Finally, 4T1 tumors treated with 55 MBq of $^{177}$Lu-FAP6-IP-DOTA responded with a ~43% decrease in growth (**Fig. 6C**). Overall survival was significantly prolonged by at least 12 days at the respective doses without inducing persistent weight loss.

To further explore the potential toxicity of a single dose of $^{177}$Lu-FAP6-IP-DOTA, tissues from mice treated with 18 MBq or 55 MBq were prepared for histological examination. No diagnostic lesions or other significant morphologic differences between treated and control mice were identified (**Supplemental Table 2**). Hepatic extramedullary hematopoiesis and increases of circulating neutrophils were observed in several of the 18 MBq-treated mice, but this is an expected finding in mice regardless of treatment received **(*26*)**. Surprisingly, 55 MBq-treated mice showed fewer histopathological changes in heart and liver than untreated controls. While mild lesions were observed in several kidneys, they were deemed nonspecific (see representative photomicrographs of tissue sections after both doses in **Supplemental Fig. 13**). One lesion observed in the myocardium of a mouse 21 days after treatment with a 55 MBq-dose revealed the presence of mineralization and epicarditis. Although this inflammation may be drug-related, carditis can be simply spontaneous **(*27*)**. The minimal radioactivity in the heart and the mouse's healthy weight gain both raise a question regarding any causal relationship between the treatment and the lesion. Taken together, these data demonstrate that the radiation doses employed here were able to suppress tumor growth without causing acute tissue changes.

## DISCUSSION

Most preclinical studies of FAP-targeted imaging and therapeutic agents to date have employed murine tumor models in which the cancer cells themselves directly express FAP **(*19,20,28-34*)**. As shown in **Fig. 2**, FAP is either absent or weakly expressed on malignant cells

from breast, lung, colorectal, and ovarian human cancer patients. Although tumor models derived from cancer cells that were transduced to overexpress FAP can be useful for proof-of-concept studies, their high FAP expression may also obscure a need to modify the molecular design of an RLT to increase tumor accumulation in humans, e.g., the addition of an albumin-binder. Tumor models with physiologically relevant levels of FAP expression should therefore be encouraged in RLT studies intended for clinical development.

It was noteworthy that our four tumor models displayed different sensitivities to $^{177}$Lu-FAP6-IP-DOTA, according to the ranking HT29 > U87MG ≈ KB > 4T1 tumors. Although variations in FAP expression will directly influence initial uptake of our RLT and could account for some of these different radiotherapy responses, no clear correlation was observed with *in vivo* FAP staining intensity (**Supplemental Fig. 2**). Discrepancies in intrinsic resistance mechanisms such as DNA damage repair pathways may help clarify the observed radiosensitivities *in vivo*, but analysis of the growth of the four cancer cell lines *in vitro* after radiation exposure also did not reveal a direct correlation (**Supplemental Fig. 14**). Considering additional characteristics such as growth rates, vascularization, extracellular matrix densities, drug efflux pumps, and CAF distributions can all influence radiobiology **(*35*)**, we suspect that no single variable will account for the disparities observed in these four tumor models. One limitation of this work is that preclinical radiotherapy studies typically translate poorly into humans due to alterations of such characteristics in murine tumor models **(*36*)**. For RLT studies in mice to predict response rates more reliably in humans, it will be important in the future to identify tumor models that more accurately mimic the radiation resistance mechanisms and general biology of human cancers.

Motivated by previous successes in utilizing a FAP6 near-infrared dye conjugate to image seven different murine tumor models **(*13*)**, we attempted to adapt the same FAP6 ligand as a radiopharmaceutical. While the inability of FAP6-DOTA to concentrate in tumors generated by FAP-negative 4T1 cells may seem initially surprising, it should be noted that Haberkorn **(*18*)** and Pomper **(*25*)** also observed minimal uptake with FAPI conjugates when imaging pancreatic and prostate tumor models, respectively, in which the cancer cells did not directly express FAP. Because FAP6

exhibits higher affinity for FAP than FAPI **(*19,20,32*)**, is readily internalized by an endocytic mechanism **(32)**, and did not show tumor accumulation even when high mass doses of compound were administered (**Supplemental Fig. 6**), we hypothesized that the lack of tumor uptake of FAP6-DOTA was due to its rapid excretion before sufficient perfusion into the tumors. Therefore, to prolong the circulation, we inserted the iodophenyl butyryl moiety to generate FAP6-IP-DOTA, which accumulated prominently in 4T1 tumors. The net effect was (i) ~88x increase in tumor dose, (ii) >1,500 improvement in tumor-total body dosimetry ratio (**Supplemental Fig. 10**), and (iii) effective radiotherapy of four tumor models.

Whether greater improvements can still be achieved with better FAP ligands **(*14,37*)**, albumin-binders **(*34,38*)**, and/or linker modifications **(*20,23,32*)** is a question worthy of further scrutiny. The dosimetry estimates of FAP6-IP-DOTA revealed most tumor-to-healthy organ ratios to be favorable (**Supplemental Fig. 10**), but the 2:1 tumor-to-kidney ratio may require additional improvement **(*39*)**. This can be achieved by altering the albumin-binder as described by others **(*38,40*)**, but one limitation of drug development is that translating optimal pharmacokinetics in mice to humans is complicated by differences in metabolism and excretion **(*10*)**. Another aspect of drug development is evaluating the performance of the FAP6-IP-DOTA candidate with respect to other FAP-targeted RLTs. FAP6-IP-DOTA demonstrates seemingly superior tumor retention compared to FAPI-46 and faster clearance from healthy organs than other FAP-targeted albumin-binding radioligands **(*19,20,30,32*)**. However, direct comparisons should be limited as most other studies employed different tumor models in which the cancer cells directly overexpressed FAP and necessitated immunocompromised mouse strains. What structural elements result in optimal properties for FAP-targeted RLT in humans remains an important question for research.

Finally, it should be noted that tumors characterized by lower numbers of FAP-positive cells could still be less responsive to an optimized FAP-targeted RLT. Thus, successful treatment of some solid tumors may require (i) combining with conventional therapies, (ii) combining with an orthogonal RLT targeted to other cells in the same tumor, and/or (iii) using a FAP-targeted radioimaging companion diagnostic to select only patients with high FAP expression for

radiotherapy **(*5,41*)**. With these improvements, it remains conceivable that a FAP-targeted RLT could prove useful for treatment of many solid tumors.

## CONCLUSIONS

To design a more clinically relevant study, four different tumor models with ostensibly physiological (i.e., lower) levels of FAP expression were selected after analysis of scRNA-seq data from human cancers. The FAP6-IP-DOTA molecule demonstrated high affinity for FAP and prolonged circulation, resulting in strong accumulation in all four tumors and significant suppression of tumor growth when radiolabeled with lutetium-177. The data suggest that $^{177}$Lu-FAP6-IP-DOTA could potentially be optimized for human use.

## DISCLOSURE STATEMENT

Spencer D. Lindeman, Ramesh Mukkamala, Madduri Srinivasarao, and Philip S. Low hold a patent on FAP-targeted radioligand therapy. Other authors declare no potential conflicts of interest.


## ACKNOWLEDGMENTS

The authors acknowledge Dr. James A. Schaber and the Purdue Imaging Facility for assistance with SPECT/CT; Kristina Grayson and the Bindley Science Center for cell sorting; MacKenzie McIntosh and the Purdue Histology Research Laboratory for preparation of mouse tissue samples and histology work; Dr. Isabelle F. Vanhaezebrouck and the Purdue University College of Veterinary Medicine for irradiation of cell samples. S.D.L thanks Jackson N. Moss, Taylor C. Schleinkofer, and Kate A. Kragness for their help with the studies.

**KEY POINTS**

QUESTION: Can a FAP-targeted radioligand therapy demonstrate sufficient safety and efficacy for preclinical development in murine tumor models in which FAP expression is limited to cancer-associated fibroblasts?

PERTINENT FINDINGS: Single-cell RNAseq data on 34 human breast, lung, ovarian, and colon cancers demonstrated that ~5% of all cells in human tumors overexpress FAP. $^{177}$Lu-FAP6-IP-DOTA successfully treated multiple murine tumor models generated from FAP-negative cancer cells.

IMPLICATIONS FOR PATIENT CARE: These data suggest that $^{177}$Lu-FAP6-IP-DOTA constitutes a promising candidate for development of FAP-targeted radiotherapy for solid tumors.

## REFERENCES


**1.** Liu R, Li H, Liu L, et al. Fibroblast activation protein: a potential therapeutic target in cancer. *Cancer Biol Ther.* 2012;13:123-129.

**2.** Garin-Chesa P, Old LJ, Rettig WJ. Cell surface glycoprotein of reactive stromal fibroblasts as a potential antibody target in human epithelial cancers. *Proc Natl Acad Sci.* 1990;87:7235-7239.

**3.** Kratochwil C, Flechsig P, Lindner T, et al. $^{68}$Ga-FAPI PET/CT: Tracer uptake in 28 different kinds of cancer. *J Nucl Med.* 2019;60:801-805.

**4.** Ferdinandus J, Fragoso Costa P, Kessler L, et al. Initial clinical experience with $^{90}$Y-FAPI-46 radioligand therapy for advanced stage solid tumors: a case series of nine patients. *J Nucl Med.* 2021;63:727-734.

**5.** Baum RP, Schuchardt C, Singh A, et al. Feasibility, biodistribution and preliminary dosimetry in peptide-targeted radionuclide therapy (PTRT) of diverse adenocarcinomas using $^{177}$Lu-FAP-2286: First-in-human results. *J Nucl Med.* 2021;63:415-423.

**6.** Dumelin CE, Trüssel S, Buller F, et al. A portable albumin binder from a DNA-encoded chemical library. *Angew Chem Int Ed.* 2008;47:3196-3201.

**7.** Müller C, Struthers H, Winiger C, et al. DOTA conjugate with an albumin-binding entity enables the first folic acid–targeted $^{177}$Lu-radionuclide tumor therapy in mice. *J Nucl Med.* 2013;54:124-131.

**8.** Kuo H-T, Merkens H, Zhang Z, et al. Enhancing treatment efficacy of $^{177}$Lu-PSMA-617 with the conjugation of an albumin-binding motif: Preclinical dosimetry and endoradiotherapy studies. *Mol Pharm.* 2018;15:5183-5191.

**9.** Tian R, Jacobson O, Niu G, et al. Evans Blue attachment enhances somatostatin receptor subtype-2 imaging and radiotherapy. *Theranostics.* 2018;8:735-745.

**10.** Kramer V, Fernández R, Lehnert W, et al. Biodistribution and dosimetry of a single dose of albumin-binding ligand [177Lu]Lu-PSMA-ALB-56 in patients with mCRPC. *Eur J Nucl Med Mol Imaging.* 2021;48:893-903.

**11.** Qian J, Olbrecht S, Boeckx B, et al. A pan-cancer blueprint of the heterogeneous tumor microenvironment revealed by single-cell profiling. *Cell Res.* 2020;30:745-762.

**12.** SCope tutorial: Pan-cancer TME blueprint. August 3, 2021; http://scope.lambrechtslab.org/#/a0f9b96f-e2d9-4156-9899-993e37a62c03/Breast.loom/tutorial. Accessed February 15, 2022.

**13.** Mukkamala R, Lindeman SD, Kragness KA, et al. Design and characterization of fibroblast activation protein targeted pan-cancer imaging agent for fluorescence-guided surgery of solid tumors. *J Mater Chem B.* 2022;10:2038-2046.

**14.** Roy J, Hettiarachchi SU, Kaake M, et al. Design and validation of fibroblast activation protein alpha targeted imaging and therapeutic agents. *Theranostics.* 2020;10:5778-5789.

**15.** Cheng JD, Dunbrack RL, Jr., Valianou M, et al. Promotion of tumor growth by murine fibroblast activation protein, a serine protease, in an animal model. *Cancer Res.* 2002;62:4767-4772.

**16.** Venning FA, Zornhagen KW, Wullkopf L, et al. Deciphering the temporal heterogeneity of cancer-associated fibroblast subpopulations in breast cancer. *J Exp Clin Cancer Res.* 2021;40:175.

**17.** Moon ES, Elvas F, Vliegen G, et al. Targeting fibroblast activation protein (FAP): next generation PET radiotracers using squaramide coupled bifunctional DOTA and DATA$^{5m}$ chelators. *EJNMMI radiopharm chem.* 2020;5:19.

**18.** Watabe T, Liu Y, Kaneda-Nakashima K, et al. Theranostics targeting fibroblast activation protein in the tumor stroma: $^{64}$Cu- and $^{225}$Ac-labeled FAPI-04 in pancreatic cancer xenograft mouse models. *J Nucl Med.* 2020;61:563-569.

**19.** Xu M, Zhang P, Ding J, et al. Albumin binder–conjugated fibroblast activation protein inhibitor radiopharmaceuticals for cancer therapy. *J Nucl Med.* 2021;63:952-958.

**20.** Wen X, Xu P, Shi M, et al. Evans blue-modified radiolabeled fibroblast activation protein inhibitor as long-acting cancer therapeutics. *Theranostics.* 2022;12:422-433.

**21.** Liu Y, Watabe T, Kaneda-Nakashima K, et al. Fibroblast activation protein targeted therapy using [$^{177}$Lu]FAPI-46 compared with [$^{225}$Ac]FAPI-46 in a pancreatic cancer model. *Eur J Nucl Med Mol Imaging.* 2022;49:871-880.

**22.** Kelly JM, Jeitner TM, Ponnala S, et al. A trifunctional theranostic ligand targeting fibroblast activation protein-α (FAPα). *Mol Imaging Biol.* 2021;23:686-696.

**23.** Meng L, Fang J, Zhao L, et al. Rational Design and Pharmacomodulation of Protein-Binding Theranostic Radioligands for Targeting the Fibroblast Activation Protein. *J Med Chem.* 2022;65:8245-8257.

**24.** Tsai T-Y, Yeh T-K, Chen X, et al. Substituted 4-carboxymethylpyroglutamic acid diamides as potent and selective inhibitors of fibroblast activation protein. *J Med Chem.* 2010;53:6572-6583.

**25.** Slania SL, Das D, Lisok A, et al. Imaging of fibroblast activation protein in cancer xenografts using novel (4-Quinolinoyl)-glycyl-2-cyanopyrrolidine-based small molecules. *J Med Chem.* 2021;64:4059-4070.

**26.** Mende N, Laurenti E. Hematopoietic stem and progenitor cells outside the bone marrow: where, when, and why. *Exp Hematol.* 2021;104:9-16.

**27.** Glass AM, Coombs W, Taffet SM. Spontaneous cardiac calcinosis in BALB/cByJ mice. *Comp Med.* 2013;63:29-37.

**28.** Fischer E, Chaitanya K, Wüest T, et al. Radioimmunotherapy of fibroblast activation protein positive tumors by rapidly internalizing antibodies. *Clin Cancer Res.* 2012;18:6208-6218.

**29.** Zboralski D, Osterkamp F, Simmons A, et al. Preclinical evaluation of FAP-2286, a peptide-targeted radionuclide therapy (PTRT) to fibroblast activation protein alpha (FAP). *Ann Oncol.* 2020;31:S488.

**30.** Zhang P, Xu M, Ding J, et al. Fatty acid-conjugated radiopharmaceuticals for fibroblast activation protein-targeted radiotherapy. *Eur J Nucl Med Mol Imaging.* 2022;49:1985-1996.

**31.** Lindner T, Loktev A, Altmann A, et al. Development of quinoline-based theranostic ligands for the targeting of fibroblast activation protein. *J Nucl Med.* 2018;59:1415-1422.

**32.** Loktev A, Lindner T, Burger E-M, et al. Development of fibroblast activation protein–targeted radiotracers with improved tumor retention. *J Nucl Med.* 2019;60:1421-1429.

**33.** Galbiati A, Zana A, Bocci M, et al. A novel dimeric FAP-targeting small molecule-radio conjugate with high and prolonged tumour uptake. *J Nucl Med.* 2022:jnumed.122.264036.

**34.** Lin J-J, Chuang C-P, Lin J-Y, et al. Rational Design, Pharmacomodulation, and Synthesis of [$^{68}$Ga]Ga-Alb-FAPtp-01, a Selective Tumor-Associated Fibroblast Activation Protein Tracer for PET Imaging of Glioma. *ACS Sens.* 2021;6:3424-3435.

**35.** Henke E, Nandigama R, Ergün S. Extracellular Matrix in the Tumor Microenvironment and Its Impact on Cancer Therapy. *Front Mol Biosci.* 2020;6:1-24.

**36.** Koontz BF, Verhaegen F, De Ruysscher D. Tumour and normal tissue radiobiology in mouse models: how close are mice to mini-humans? *Br J Radiol.* 2016;90:20160441.

**37.** Hettiarachchi SU, Li Y-H, Roy J, et al. Targeted inhibition of PI3 kinase/mTOR specifically in fibrotic lung fibroblasts suppresses pulmonary fibrosis in experimental models. *Sci Transl Med.* 2020;12:eaay3724.

**38.** Kuo H-T, Lin K-S, Zhang Z, et al. Novel $^{177}$Lu-labeled Albumin-binder-conjugated PSMA-targeting Agents with Extremely High Tumor Uptake and Enhanced Tumor-to-kidney Absorbed Dose Ratio. *J Nucl Med.* 2020;62:521-527.

**39.** Emami B, Lyman J, Brown A, et al. Tolerance of normal tissue to therapeutic irradiation. *Int J Radiat Oncol Biol Phys.* 1991;21:109-122.

**40.** Umbricht CA, Benešová M, Schibli R, et al. Preclinical Development of Novel PSMA-Targeting Radioligands: Modulation of Albumin-Binding Properties To Improve Prostate Cancer Therapy. *Mol Pharm.* 2018;15:2297-2306.

**41.** Fendler WP, Pabst KM, Kessler L, et al. Safety and Efficacy of $^{90}$Y-FAPI-46 Radioligand Therapy in Patients with Advanced Sarcoma and Other Cancer Entities. *Clin Cancer Res.* 2022;28:4346-4353.

## FIGURES

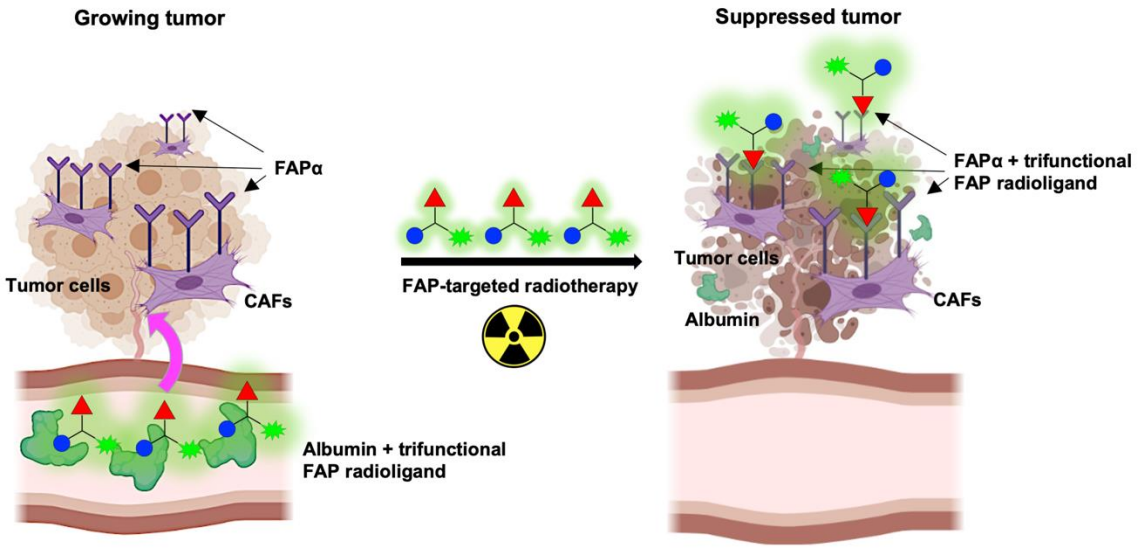


**FIGURE 1.** Radiolabeled FAP6-IP-DOTA circulates for a prolonged period due to the affinity of iodophenyl-butyric acid (●) for serum albumin. This enables the conjugate to perfuse the poorly vascularized solid tumors so the ligand (▲) may bind to FAP receptors on CAFs. The chelated radionuclide (✹) emits radiation that induces DNA strand breaks inside the tumor cells, thereby suppressing tumor growth.

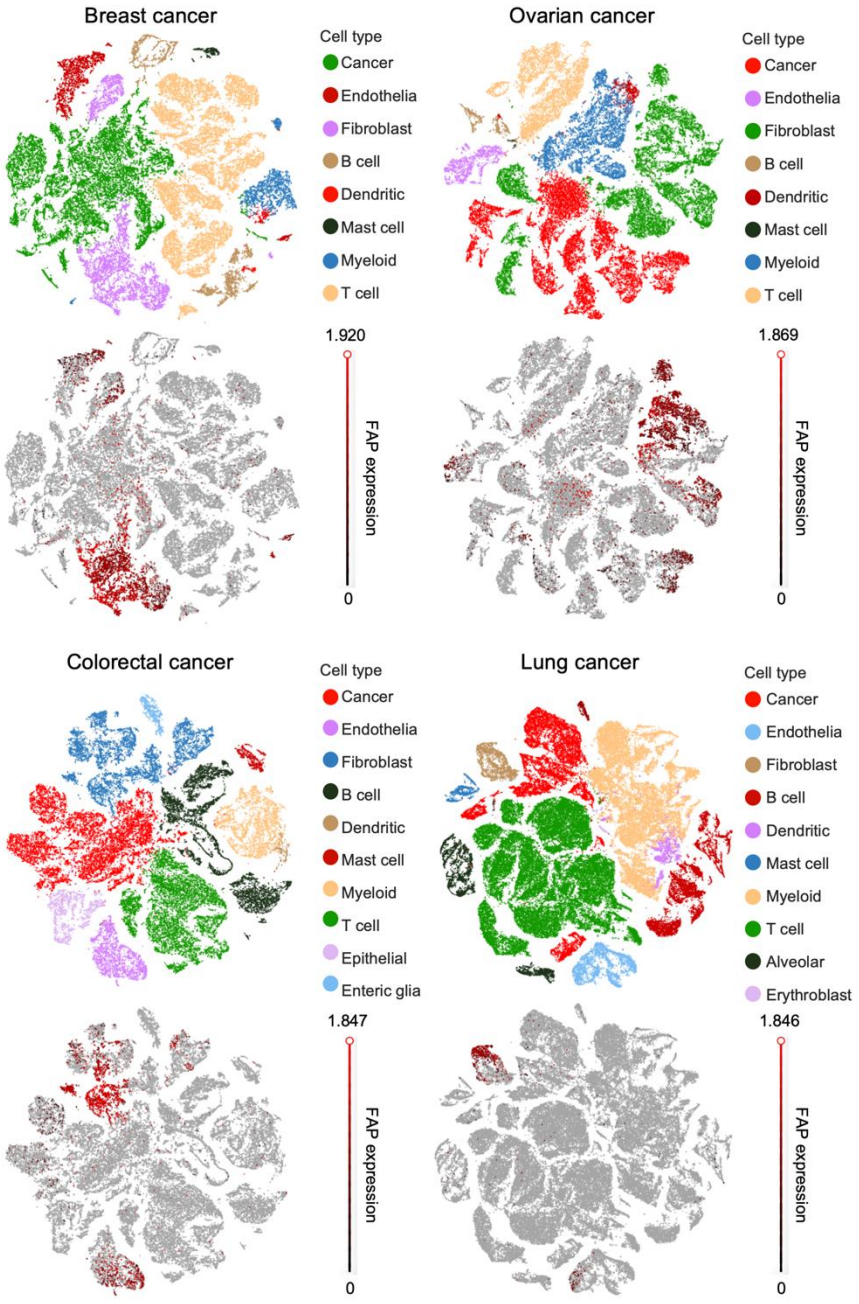


**FIGURE 2.** t-distributed Stochastic Neighbor Embedding (t-SNE) plots of single-cell RNA sequencing data from human breast, ovarian, colorectal, and lung cancers.

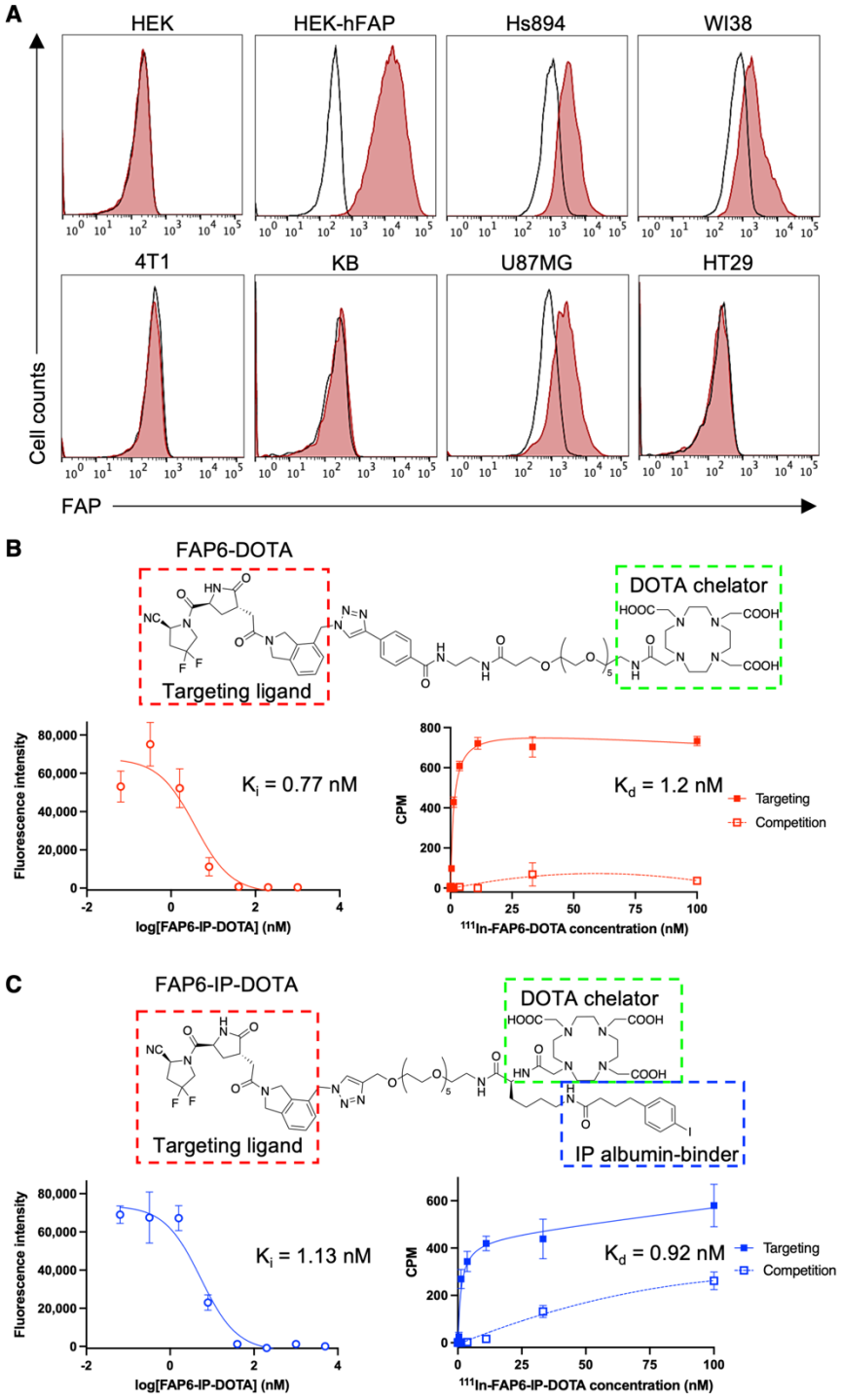


**FIGURE 3.** (**A**) Histograms of FAP expression by the indicated cell lines (unstained controls = black; anti-FAP stained cells = red). Structures, HEK-hFAP competition assays, and Hs894 CAF binding assays of (**B**) FAP6-DOTA and (**C**) FAP6-IP-DOTA.

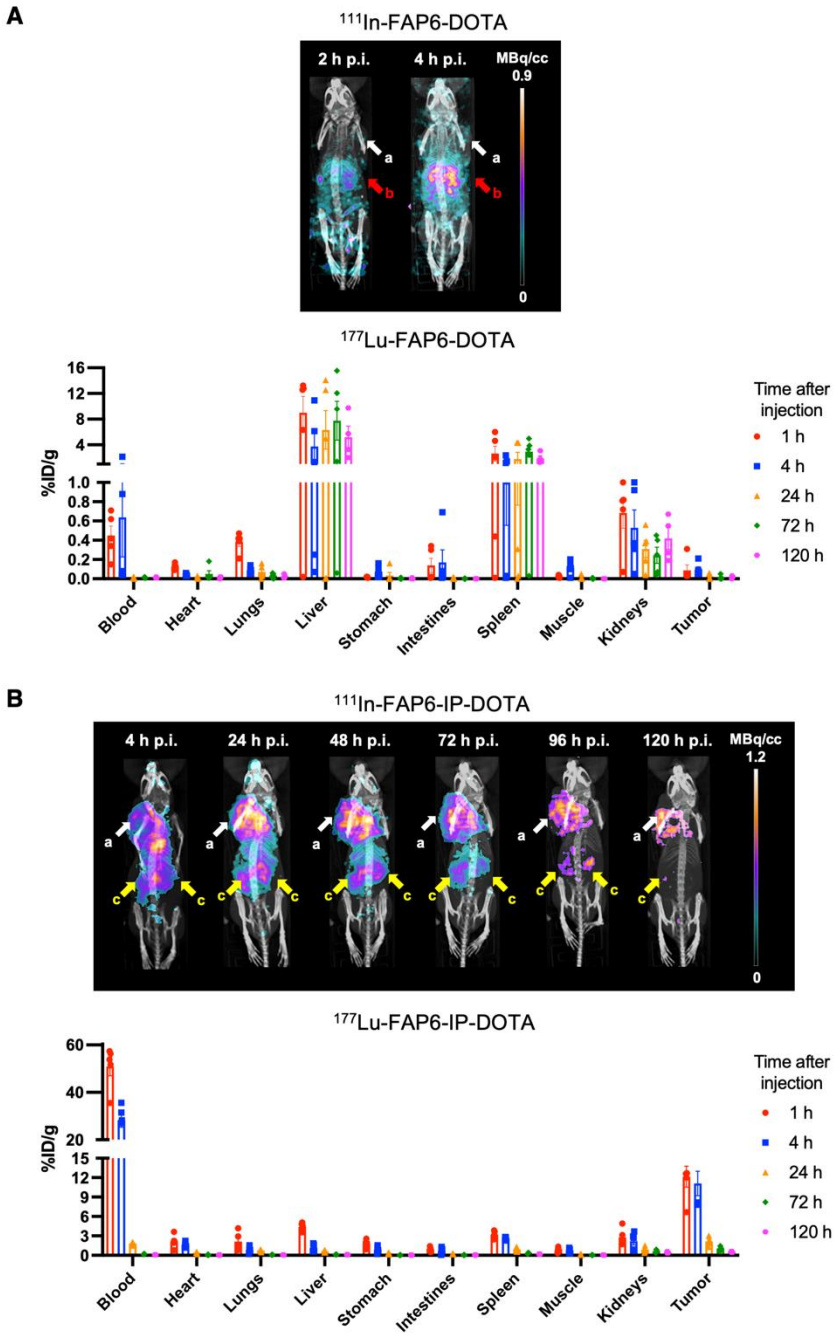


**FIGURE 4.** SPECT/CT and biodistribution analyses of (**A**) FAP6-DOTA vs. (**B**) FAP6-IP-DOTA in 4T1 tumors. Arrows: a=tumors; b=liver; c=kidneys.

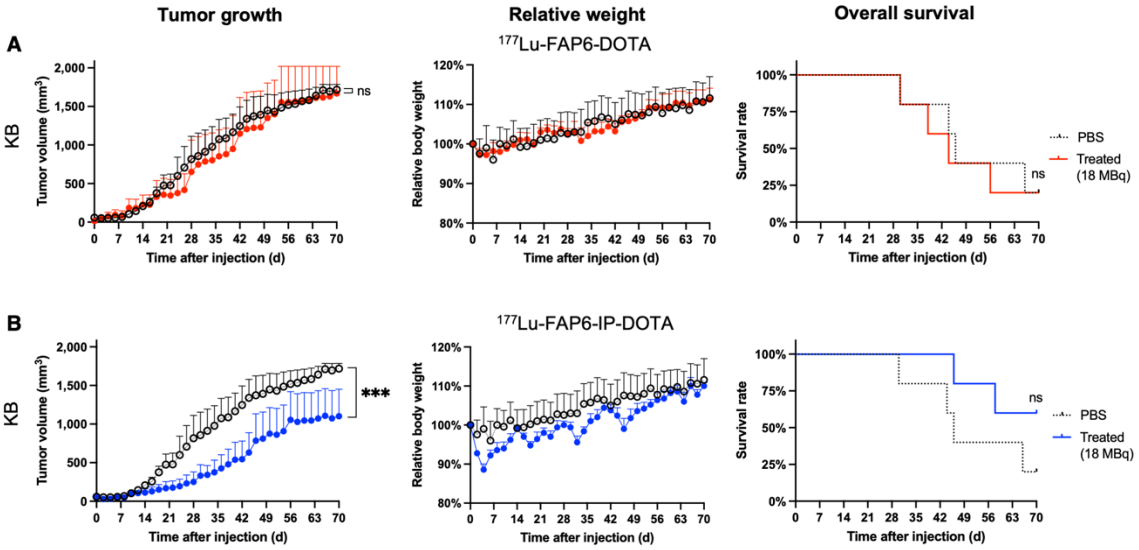


**FIGURE 5.** Treatment of KB tumors with (**A**) $^{177}$Lu-FAP6-DOTA, or (**B**) $^{177}$Lu-FAP6-IP-DOTA (n=5/group).

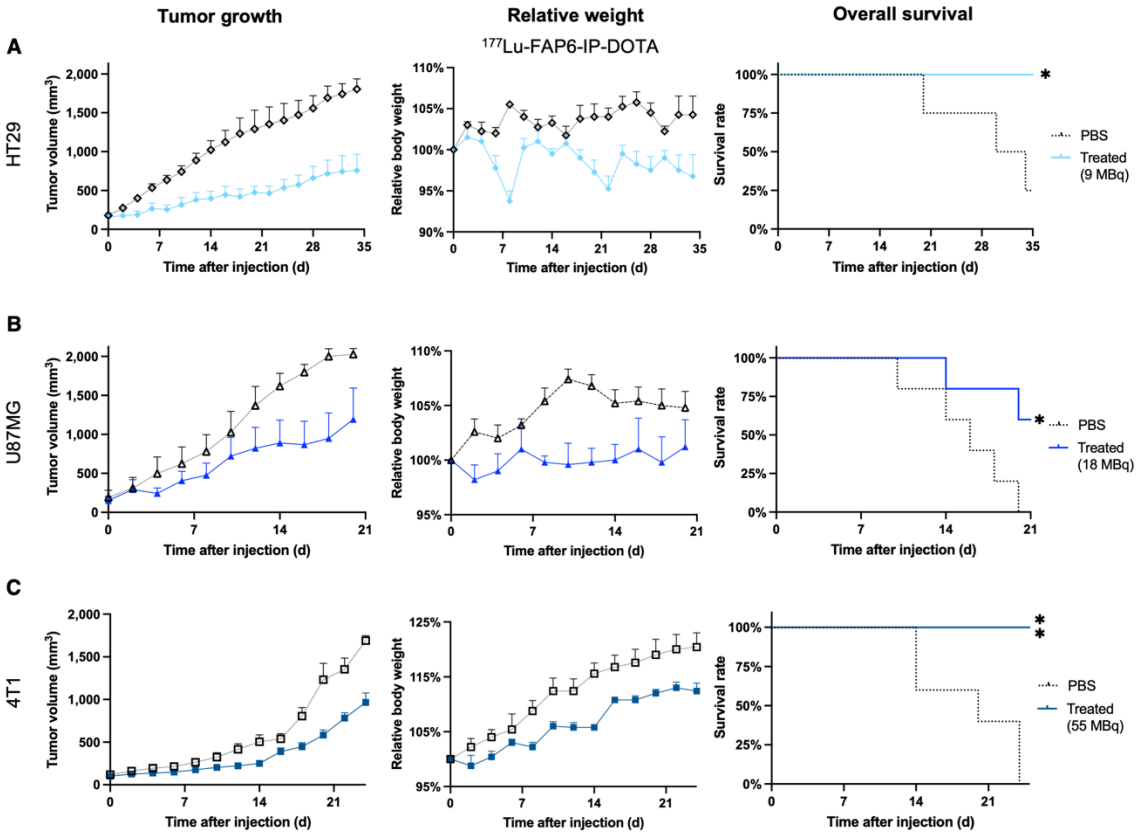


**FIGURE 6.** Treatment of (**A**) HT29 (n=4/group), (**B**) U87MG (n=5/group), or (**C**) 4T1 (n=5/group) tumors with $^{177}$Lu-FAP6-IP-DOTA.

## Graphical Abstract

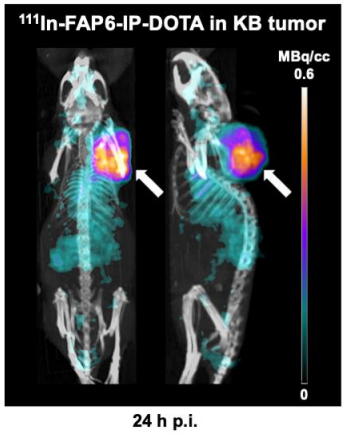


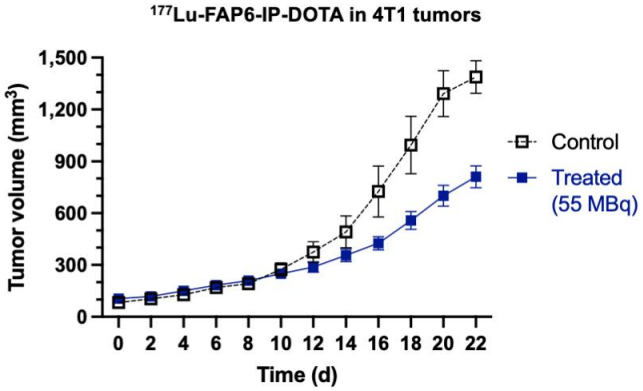

**Fibroblast activation protein targeted radioligand therapy for treatment of solid tumors**

## SUPPLEMENTAL DATA

## MATERIALS & METHODS

### Materials

Each cell line was originally purchased from ATCC. Cell culture media such as Eagle's Minimum Essential Medium (EMEM), Dulbeco's Modified Eagle's Medium (DMEM) and Roswell Park Memorial Institute medium 1640 (RPMI-1640) were purchased from GIBCO. All other cell culture reagents such as fetal bovine serum (FBS), penicillin-streptomycin, and 2 mM glutamine were purchased from Life Technologies. Amine-coated 24-well cultureware plates were obtained from BD Biosciences (San Jose, CA). Accutase was acquired from BioLegend (San Diego, CA). Human FAP APC-conjugated (Catalog No. FAB3715A-100) and murine FAP monoclonal rat IgG (Catalog No. MAB9727-SP) antibodies were procured from R&D Systems (Minneapolis, MN). Common cell culture materials such as culture flasks and syringes were purchased from VWR (Chicago, IL). Fluorescence based assays were measured with a BioTek Synergy Neo2 plate reader. Flow cytometry was analyzed using an Attune NxT Acoustic Focusing Flow Cytometer**.** LRMS-LC/MS was performed with an Agilent 1220 Infinity LC with a reverse-phase XBridge Shield RP18 column (3.0 x 50 mm, 3.5 µm). Radiolabeling was achieved using a Fisherbrand Isotemp Digital Dry Bath/Block Heater (Waltham, MA). Radio-HPLC analysis was performed with an Agilent 1260 Infinity II equipped with a Flow-RAM detector purchased from LabLogic (Brandon, FL) and a reverse-phase XBridge Shield RP18 column (3.0 x 50 mm, 3.5 µm). SPECT/CT scans were acquired with a VECTor/CT system with a clustered multi-pinhole high-energy collimator (MILabs, Utrecht, The Netherlands). Radioactive binding and biodistribution studies were measured with a Packard Cobra Gamma Counter (Niederösterreich, Austria).

### Synthesis

4-methyl isoindoline-4-carboxylate hydrochloride was purchased from PharmaBlock (Hatfield, PA). Boc-L-pyroglutamic acid benzyl ester was purchased from Accela ChemBio (San Diego, CA). 4-(*p*-iodophenyl)butyric acid was purchased from AstaTech, Inc (Bristol, PA). NHS-ester-$PEG_6$-NHFmoc and Propargyl-$PEG_6$-amine were purchased from BroadPharm. DOTA-NHS ester was purchased from

Macrocyclics. Lysine was purchased from AAPPTec (Louisville, KY). Fmoc-L-Lys-OtBu hydrochloride, 4,4-Difluoro-L-prolinamide hydrochloride, and HATU were purchased from Chem-Impex International (Chicago, IL). 4-Ethynylbenzoic acid and mono-Fmoc ethylene diamine hydrochloride were purchased from AA Blocks LLC (San Diego, CA). Di-tert-butyl dicarbonate was purchased from Oakwood Chemical (Estill, SC). Palladium, 10% on carbon, was purchased from Alfa Aesar (Haverhill, MA). Sodium borohydride, N-bromosuccinimide, triphenylphosphine, sodium azide, lithium bis(trimethylsilyl)amide, tert-butyl-bromoacetate, 1,8-diazabicyclo[5.4.0]undec7-ene, pyridine, imidazole, phosphoryl chloride, diethyl either, DIPEA, TFA, THF, DMF, DCM, MeOH, DMSO, and all other reagents were purchased from Sigma-Aldrich (St. Louis, MO). All synthesized molecules were purified using either flash chromatography (CombiFlash RF, Teledyne) or RP-HPLC (Agilent 1200 Instrument) with an XBridge OBD preparative column (19 x 150 mm, 5 µm) purchased from Waters (Milford, MA).

**Analyses of FAP Expression by Single Cell RNA-seq**

We exploited scRNA-seq data published by Qian et al (*1*) that profiled the transcriptomes of more than 233,000 single cells from 34 cancer patients. For our purposes, FAP overexpression data on tumor cells collected from fourteen breast cancer patients (44,026 cells), five ovarian cancer patients (45,115 cells), seven colorectal cancer patients (41,758 cells), and eight lung cancer patients (88,668 total cells) from the VIB KU Leuven Center for Cancer Biology database were analyzed by following SCope tutorials (*2*). All cell types were selected using the lasso tool and the corresponding metadata were downloaded and analyzed. A FAP expression level = 0 was considered FAP-negative, while a FAP expression level > 0 was considered FAP-positive.

**Cell Culture and Sorting**

Cell cultures were maintained in DMEM (HEK and Hs894 cells), EMEM (HT1080 and U87MG cells) or RPMI-1640 supplemented with 1% 2 mM glutamine (4T1 and KB cells) at 37°C in a 5% $CO_2$ and 95% humidified atmosphere. 10% FBS and 1% penicillin-streptomycin were added to all media. Generation, characterization, and culture of HT1080-hFAP cells were previously reported (*3*). Regular screening for mycoplasma contamination was performed to ensure integrity of all studies, and contaminated cultures were discarded. HEK-hFAP cells with high levels of FAP expression were isolated by cell sorting using an

anti-human FAP monoclonal antibody and a BD LSRFortessa Flow Cytometer. The high FAP expressing cells were cultured and stored for subsequent confocal and binding studies.

**Radiosynthesis and Formulation**

Stock solutions of FAP6 conjugates were diluted in ammonium acetate (0.5 M, pH 8.0) to 0.5 mM. Radio-HPLC method = (A) 20 mM ammonium bicarbonate buffer (pH 7) and (B) acetonitrile in a linear gradient from 5% B to 95% B over 15 minutes. After confirmation of successful radiolabeling by radio-HPLC analysis (radiopurity > 95%, radiochemical yield > 90%), sodium-diethylenetriamine pentaacetate (DTPA-Na) solution (5 mM, pH 7.0) was added at a final concentration of 0.2 mM to complex any unreacted traces of radioactive isotope. Conjugates were formulated in 5% ethanol in PBS (v/v) containing 10% sodium ascorbate (w/v) and 0.5% L-methionine (w/v) for all *in vitro* and *in vivo* studies.

**Whole-Cell Assays**

*Flow Cytometry*. Samples containing ~100,000 cells were suspended in staining buffer (2% FBS in PBS) and incubated for 20 minutes on ice with FAP antibodies (1:100 dilution), then washed with fresh solution three times. Murine cell lines were further stained with an APC-conjugated secondary antibody and washed in similar fashion. Cells were then resuspended in staining buffer for flow cytometry analysis. Singlet cells were gated via FSC and SSC examination, and FAP-positive subpopulations were established by non-staining controls on the RL1 channel. Final figures were generated using FlowJo (version 10.8) software.

*Displacement Assay*. 250,000 HEK-hFAP cells were seeded per well into amine-coated 24-well plates and allowed to reach confluence before they were incubated with 10 nM FAP6-rhodamine (*3*) in the presence of increasing concentrations of FAP6-DOTA or FAP6-IP-DOTA. After incubation for one hour at 4°C, the cells were washed three times with PBS to remove unbound fluorescence and dissolved in 1% SDS. The samples were then transferred to 96-well, clear bottom, black wall plates and cell-bound fluorescence was measured with a BioTek Synergy Neo2 plate reader. Wavelengths were set to $\lambda_{ex}$ = 552 nm and $\lambda_{em}$ = 575 nm and cell-bound fluorescence was plotted against the logarithm of the concentrations of the FAP6 conjugates in nM. A $K_d$ of 2.67 nM for FAP6-rhodamine was used to calculate the $K_i$ of the FAP6 conjugates using one-site binding nonlinear fit. All samples were performed in triplicate.

*Direct Binding*. 100,000 Hs894 CAFs were seeded in 24-well plates and allowed to grow to confluence prior to the addition of either $^{111}$In-FAP6-DOTA or $^{111}$In-FAP6-IP-DOTA in the absence or presence of

excess FAP6 ligand (to competitively block radioactive binding). After incubation for 1h at room temperature, the cells were washed three times with PBS to remove unbound radioactivity and dissolved in 1.0 M NaOH. The samples were then transferred to tubes and cell-bound radioactivity was measured using a gamma counter. A specific binding constant was calculated using one-site specific binding nonlinear regression after subtracting competition counts from total binding counts. All samples were performed in triplicate.

*Internalization.* 200,000 HT1080-hFAP cells were seeded into each well of 24-well plates and grown to confluence. The media was removed, and 25 nM of $^{111}$In-FAP6-DOTA or $^{111}$In-FAP6-IP-DOTA in 0.25 mL of media containing 1% FBS was added to all wells. The plates were incubated at 37ºC for the indicated times, after which the media was removed, and the wells were washed three times with PBS to remove unbound radioactivity. To determine the total radioactivity absorbed by the cell, a subset of samples was immediately lysed with 1.0 M NaOH. Additional samples were incubated for 1 minute with HEPES buffer (pH 2.5) to remove surface-bound radioactivity, after which the cells were dissolved with 1.0 M NaOH to harvest the internalized radioactivity. All samples were transferred to tubes for gamma counter measurements, and internalized radioactivity was normalized as a percent of total absorbed radioactivity by the cells. All samples were performed in triplicate.

*Radiosensitivity*. 100,000 4T1, HT29, KB, or U87MG cells were seeded into 12 well plates and then promptly irradiated while still suspended (i.e., before the cells adhered to the bottom of the wells). Doses of 2, 4, 8, 12, and 20 Gy were administered with a photon beam from a 6MV Linac (Varian EX). A 1.5 cm bolus was placed underneath the plates for full electron equilibrium. Confluency of the cells were visually estimated every other day to gauge relative radiosensitivities of the difference cell lines. All samples were performed in triplicate.

**Animals**

6-week-old (16-19 g) female Balb/c mice were purchased from Charles River. 12-week-old female athymic nu/nu mice (23-27 g) were purchased from Envigo. Up to 5 mice were housed in a single cage with corn cob bedding and paper strips for enrichment. Temperatures and humidity were maintained at 21–22°C and 30–70%, respectively, throughout all studies. Prior to initiation of studies, mice were housed in cages on ventilated racks with filtered air, which were changed biweekly. Upon initiation of studies, mice were

housed in static cages, which were changed weekly. All tumor cells (4T1, KB, HT29, and U87MG) were suspended in PBS at time of inoculation in appropriate mouse breeds. Nu/nu mice were inoculated on their shoulder with 5 x $10^6$ cells of HT1080-FAP cells for specificity studies.

**SPECT/CT Scans**

Tumors were allowed to grow up to ~1 $cm^3$ before initiating SPECT/CT studies. Mice were injected intravenously via the lateral tail vein with 1-30 nmol of FAP6-DOTA or FAP6-IP-DOTA radiolabeled with $^{111}$In (~10 MBq) or $^{177}$Lu (~55 MBq) in 100 µL of vehicle. FAP6 conjugates were radiolabeled at a specific activity of ~2 MBq/nmol for $^{111}$In or ~11 MBq/nmol for $^{177}$Lu, unless indicated otherwise. Immediately prior to initiation of the scans, mice were anesthetized by inhalation of ~3% isoflurane using a 1.25 L/min flow rate of oxygen and maintained at these conditions on top of a heating strip to regulate murine body temperatures in the prone position without additional fixation for the duration of the scan. The SPECT scans were acquired with a 0.35 mm pinhole (mouse whole body) collimator, 15–60 second acquisitions per bed position across ~50 bed positions, totaling 20–60 minutes per mouse. The CT scans were acquired with an X-ray source set at 60 kV and 615 µA. The SPECT images were reconstructed with U-SPECT II software using $^{111}$In γ-energy windows of 171 and 241 keV or $^{177}$Lu γ-energy window of 208 keV. A POS-EM algorithm was used with 16 subsets and 4 iterations on a 0.8 mm voxel grid. A 3.0 median filter was applied to all scans. Background remover was only applied to remove low levels of noise observed outside the bodies of the mice. Bladders were masked as needed within the first 24 hours to enable visualization of the biodistribution of the FAP6-targeted radiotracers.

**Radioactive Biodistribution**

4T1 tumors were allowed to grow to ~250–500 $mm^3$ before initiating biodistribution studies. Each tumor-bearing mouse was intravenously injected via the lateral tail vein with 5 nmol of FAP6-DOTA radiolabeled with $^{177}$Lu (~3.7 MBq) or 5 nmol of FAP6-IP-DOTA radiolabeled with $^{111}$In (~0.37 MBq) or $^{177}$Lu (~3.7 MBq) in 100 µL of vehicle. Mice were euthanized by $CO_2$ asphyxiation at 1, 4, 24, 72, or 120 hours post injection. Organs were thoroughly washed with buffer to remove excess blood before gamma counter analysis. Results were decay corrected then normalized as percentages of the injected dose per gram of tissue (%ID /g) and provided as mean ± standard error.

**Dosimetry Calculations**

All absorbed doses were calculated with OLINDA 2.2.3 software using the *ex vivo* biodistribution data from Fig. 4B and 4D. Estimates for healthy organs were calculated assuming a 25 g mouse phantom. Tumor dose estimates were calculated with the sphere model. Time-activity curves were fitted to the biodistribution data of each organ individually with exponential functions. Estimates for healthy organs were calculated assuming a 25 g mouse phantom.

**Radiotherapy**

4T1, HT29, KB, and U87MG tumors were grown to ~109 $mm^3$ (n = 5 per group), ~169 $mm^3$ (n = 4 per group), ~52 $mm^3$ (n = 5 per group), or ~173 $mm^3$ (n = 5 per group), respectively, then randomly divided into control and treatment groups. Each tumor-bearing mouse was intravenously injected via the lateral tail vein with up to 5 nmol of FAP6 conjugates radiolabeled with $^{177}Lu$ (≤ 55 MBq) in 100 µL of vehicle. Specific activities of 1.8 MBq/nmol were tested in HT29, U87MG, and 4T1 tumor-bearing mice; 3.6 MBq/nmol in U87MG, KB, and 4T1 tumor-bearing mice; 11 MBq/nmol in 4T1 tumor-bearing mice. Radioactive injections of 55 MBq were accompanied with an injection of amino acid solution (30 mg of lysine in PBS) into the intraperitoneal cavity. Furthermore, 4T1-tumor bearing mice injected with 55 MBq of $^{177}Lu$-FAP6-IP-DOTA were measured every other day by two separate people in blinded fashion (i.e., they did not know which mice were control vs. treated). Tumor volumes were calculated as 0.5 x L x $W^2$, where L is the longest axis (in millimeters), and W is the axis perpendicular to L (in millimeters). Humane endpoint criteria were defined as weight loss of more than 20% of the initial body weight, a tumor volume of more than 1,800 $mm^3$ for human xenografts or 1,500 $mm^3$ for syngeneic murine cancers, or open ulceration.

**Pathology & Histology**

Mice were randomly selected from control and treatment groups (as indicated) for further evaluation at the conclusion of the radiotherapy studies. Myocardium, liver, and kidneys were harvested, washed, fixed in a 10% formalin solution for 48-72 hours. Organs were then maintained in a 70% ethanol solution until radioactivity had fully decayed, after which they were submitted to the Histology Research Laboratory at Purdue University to be embedded in paraffin, sectioned, and stained with hematoxylin and eosin (H&E). Additional tumor samples were stained with a FAP antibody (1:150 dilution) for histopathological analysis.

**Statistical Significance**

Statistical significance in tumor sizes was analyzed by unpaired two-tailed t test (*$P < 0.05$, **$P < 0.01$, ***$P < 0.001$). Statistical significance of survival rates was determined by Log-rank (Mantel-Cox) test (*$P < 0.05$).

**FIGURES & TABLES**

**Synthesis of FAP6 Conjugates**

Synthesis of key FAP6 intermediates **4** and **9** were performed as reported previously (*3,4*).

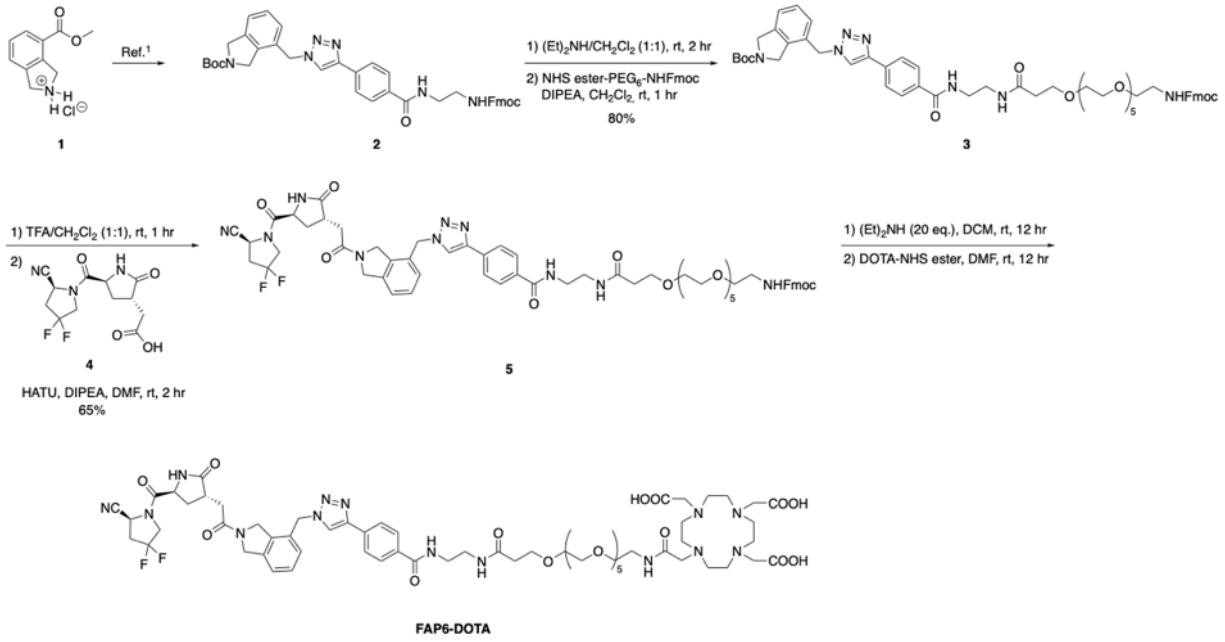


**Supplemental Scheme 1**. Synthesis of FAP6-DOTA.

**Synthesis of tert-butyl 4-((4-(4-((1-(9H-fluoren-9-yl)-3,25-dioxo-2,7,10,13,16,19,22-heptaoxa-4,26-diazaoctacosan-28-yl)carbamoyl)phenyl)-1H-1,2,3-triazol-1-yl)methyl)isoindoline-2-carboxylate (3):** Compound **2** (400mg, 0.584 mmol) was dissolved in a DCM:MeOH solution (1.0 + 0.5 mL), then $(Et)_2NH$ (1.0 mL) was added before stirring at room temperature for 2 hours. The reaction mixture was evaporated under reduced pressure and the resulting crude residue purified by flash chromatography using a DCM:MeOH mobile phase. The resulting free amine of compound **2** was dissolved in DCM (1 mL for 1 mmol) followed by NHFmoc-$PEG_6$-NHS ester (1.2 eq) and DIPEA (2.0 eq), and the resulting solution was stirred under inert atmosphere at room temperature for 2 hours. The reaction mixture was evaporated under reduced pressure and the resulting crude residue was purified by flash chromatography using a DCM:MeOH mobile phase to provide the compound **3** as white solid. LC/MS for **3**: LC/MS (m/z): calculated $[M+H]^+$ for $C_{55}H_{69}N_7O_{12}$: 1021.2, observed: 1021.2g/mol.

**Synthesis of (9H-fluoren-9-yl)methyl (1-(4-(1-((2-(2-((3S)-5-((S)-2-cyano-4,4-difluoropyrrolidine-1-carbonyl)-2-oxopyrrolidin-3-yl)acetyl)isoindolin-4-yl)methyl)-1H-1,2,3-triazol-4-yl)phenyl)-1,6-dioxo-9,12,15,18,21,24-hexaoxa-2,5-diazahexacosan-26-yl)carbamate (5):**

Compound **3** (250 mg, 0.268 mmol) was dissolved in DCM (1.0 mL) at room temperature, then TFA (0.5 mL) was added and stirred for 30 minutes. The reaction mixture was evaporated and dried under vacuum. In a separate round bottom flask the carboxylic acid-bearing compound **4** (*3*) (100 mg, 0.333 mmol) was dissolved in DMF (0.5 mL) with HATU (151 mg, 0.399 mmol), DIPEA (0.170 mL, 0.999mmol) and the reaction mixture stirred was stirred under inert atmosphere at room temperature for 10 minutes. The amine generated *in situ* from compound **3** (220 mg, 0.268 mmol) was dissolved in DMF (1 mL), added to the above reaction mixture, and stirred for 2 hours. The reaction mixture was diluted with water (15 mL) and stirred at room temperature for 15 min, after which the formed black turbidity formed was filtered then redissolved in a DCM:MeOH solution. After evaporation of the organic layer, the obtained crude residue was purified by reverse phase preparative high performance liquid chromatography (HPLC) (A= 20 mm $NH_4OAc$ buffer (pH = 7), B = $CH_3CN$, solvent gradients 5% B to 95% in 60 min provided the compound **5** as white solid. LC/MS for **5**: LC/MS (m/z): calculated $[M+H]^+$ for $C_{62}H_{72}F_2N_{10}O_{13}$: 1204.3, observed: 1204.3 g/mol.

**Synthesis of 2,2',2''-(10-(1-(4-(1-((2-(2-((3S)-5-((S)-2-cyano-4,4-difluoropyrrolidine-1-carbonyl)-2-oxopyrrolidin-3-yl)acetyl)isoindolin-4-yl)methyl)-1H-1,2,3-triazol-4-yl)phenyl)-1,6,28-trioxo-9,12,15,18,21,24-hexaoxa-2,5,27-triazanonacosan-29-yl)-1,4,7,10-tetraazacyclododecane-1,4,7-triyl)triacetic acid (FAP6-DOTA):**

Compound **5** (175 mg, 0.16 mmol) was dissolved in DCM (0.5 mL), then $(Et)_2NH$ (20 eq) was added and stirred at room temperature overnight. Reaction progress was monitored by LC/MS for complete deprotection of the Fmoc group to generate the free amine from **5:** LC/MS (m/z) calcd for: $C_{47}H_{63}F_2N_{10}O_{11}[M+H]$: 981.4 found: 981.4 g/mol. The reaction mixture was evaporated under reduced pressure and the obtained crude residue was triturated with EtOAc (2 x10 mL) then diethyl ether (3 x 10 mL), followed by filtration and dried under vacuum before further use. The free amine from compound **5** (0.03 mmol) and DOTA-NHS ester (0.045 mmol) were dissolved in anhydrous DMF (0.5 ml) was DIPEA was added (0.091 mmol) before stirring overnight. Reaction progress was monitored by LC/MS for complete

consumption of starting material, after which the reaction mixture was diluted with water (0.5 mL) and purified via RP-HPLC [A = 20 mM $NH_4OAc$ buffer (pH 7.0) and B = $CH_3CN$, solvent gradient 5% B to 35% B in 60 minutes] to yield **FAP6-DOTA**. LC/MS for **FAP6-DOTA**: LC/MS (m/z): calculated $[M+H]^+$ for $C_{63}H_{88}F_2N_{14}O_{18}$: 1368.5, observed: 1368.5 g/mol.

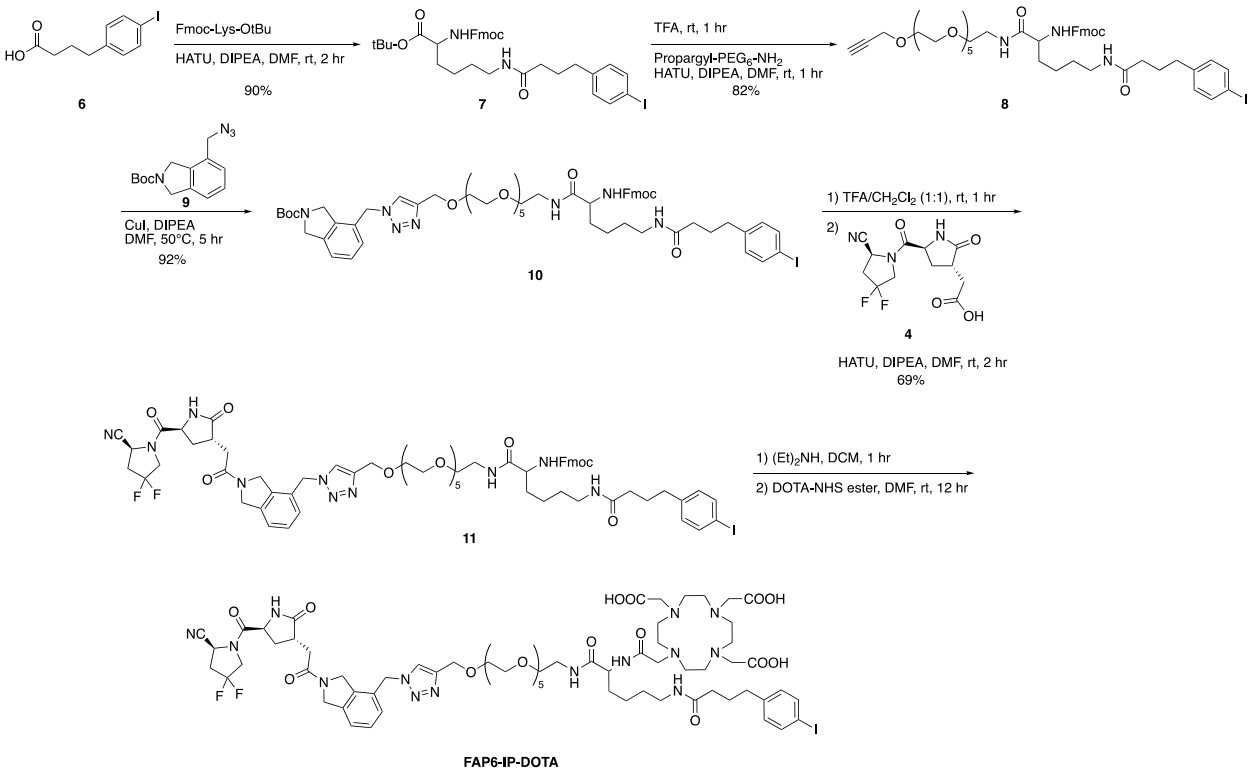


**Supplemental Scheme 2**. Synthesis of FAP6-IP-DOTA.

**Synthesis of N2-(((9H-fluoren-9-yl)methoxy)carbonyl)-N6-(4-(4-iodophenyl)butanoyl)-L-lysine (7):**

4-(*p*-iodophenyl)butyric acid (Compound **6**) (500 mg, 3.460 mmol) was dissolved in anhydrous DMF (10 mL) with HATU (1.3 g, 3.460 mmol) and anhydrous DIPEA (3 eq) then stirred for 10 minutes at room temperature under inert gas. Fmoc-Lys-OtBu HCl (1.6 g, 3.460 mmol) in anhydrous DMF (5.0 mL) and DIPEA (1.15 mL, 6.92 mmol) were added to the above reaction mixture. The resulting solution was stirred under inert atmosphere at room temperature for 2 hours as reaction progress was monitored by LC/MS. After complete consumption of the starting materials, the reaction mixture was diluted with water and extracted into EtOAc (2 x 50 mL). The combined organic layers were further washed with water (50 mL),

brine (50 mL) and dried over anhydrous magnesium sulphate. The crude product was obtained by filtration then evaporation under reduced pressure, and purified by flash chromatography using a Hex:EtOAc mobile phase to provide compound **7** as a fluffy white solid. LC/MS for **7**: LC/MS (m/z): calculated $[M+H]^+$ for $C_{31}H_{33}IN_2O_5$: 697.6, observed: 697.6 g/mol.

**Synthesis of (9H-fluoren-9-yl)methyl (R)-(33-(4-iodophenyl)-23,30-dioxo-4,7,10,13,16,19-hexaoxa-22,29-diazatritriacont-1-yn-24-yl)carbamate (8):**

Compound **7** (545 mg, 0.782 mmol) was dissolved in neat TFA and stirred for one hour. Progress of the reaction was monitored via LC/MS. LC/MS (m/z): $[M+H]^+$ calculated for $C_{31}H_{33}IN_2O_5$, 641.5; observed mass 641.5. The deprotected carboxylic acid product was isolated *en vacuo* and used without further purification, by redissolving in anhydrous DMF with HATU (1 350 mg, 0.937 mmol) and anhydrous DIPEA (0.26 mL, 1.562 mmol) for 10 minutes. Propargyl-$PEG_6$-amine (300 mg, 0.937 mmol) was dissolved in anhydrous DMF and DIPEA (0.13 mL, 0.781 mmol) and added to the above reaction mixture. The resulting solution was stirred under inert atmosphere at room temperature for 2 hours. The reaction mixture was diluted with water, extracted with EtOAc, and evaporated under reduced pressure. The crude product was purified by flash chromatography using a DCM:MeOH mobile phase to yield compound **8** as a gummy white solid. LC/MS for **8**: LC/MS (m/z): calculated $[M+H]^+$ for $C_{46}H_{60}IN_3O_{10}$: 942.9, observed: 942.9 g/mol.

**Synthesis of tert-butyl (R)-4-((4-(1-(9H-fluoren-9-yl)-5-(4-(4-(4-iodophenyl)butanamido)butyl)-3,6-dioxo-2,10,13,16,19,22,25-heptaoxa-4,7-diazahexacosan-26-yl)-1H-1,2,3-triazol-1-yl)methyl)isoindoline-2-carboxylate (10).**

To a mixture of azide **9** (*3*) (210 mg, 0.764 mmol) and alkyne **8** (600 mg, 0.636 mmol) in dry DMF (5 mL) was added CuI (0.5 eq) and DIPEA (2.0 eq). The reaction mixture was stirred under inert gas at 50°C and for 1 hour. After cooling to room temperature, the reaction mixture was isolated *en vacuo*, redissolved in DCM, and diluted with saturated aqueous ammonium chloride (20 mL). The product was then extracted with DCM (2 x 50 mL). The organic extracts were combined, washed with water and brine, then evaporated. The crude residue was purified by flash chromatography using a DCM:MeOH mobile phase to yield

compound **10** as a brown gummy solid. LC/MS for **10**: LC/MS (m/z): calculated $[M+H]^+$ for $C_{60}H_{78}IN_7O_{12}$: 1217.2, observed: 1217.2 g/mol.

**Synthesis of (9H-fluoren-9-yl)methyl ((R)-1-(1-((2-(2-((3S,5S)-5-((R)-2-cyano-4,4-difluoropyrrolidine-1-carbonyl)-2-oxopyrrolidin-3-yl)acetyl)isoindolin-4-yl)methyl)-1H-1,2,3-triazol-4-yl)-31-(4-iodophenyl)-21,28-dioxo-2,5,8,11,14,17-hexaoxa-20,27-diazahentriacontan-22-yl)carbamate (11).**

To a solution of compound **10** (500.0 mg, 0.411 mmol) in DCM (5.0 mL) at room temperature was added TFA (1.0 mL), which was stirred for 60 minutes. The reaction mixture was evaporated and dried under vacuum. In a separate round bottom flask, carboxylic acid **4** (*3*) (150.0 mg, 0.439 mmol) was dissolved in DMF (1.0 mL) followed by HATU (200.0 mg, 0.526 mmol) and DIPEA (0.18 mL), and the resulting mixture was stirred under inert gas at room temperature for 10 minutes. The amine *in situ* generated from **10** (458 mg, 0.41 mmol) was dissolved in DMF (1 mL) and added to the above reaction mixture. The resulting solution was stirred at room temperature for 2 hours, after which it was diluted with water (15 mL) and stirred at room temperature for 10 minutes. The black turbidity formed in the mixture was filtered, then redissolved in DCM:MeOH and evaporated. The crude residue was purified by reverse phase preparative high performance liquid chromatography (RP-HPLC) [A = 20 mM $NH_4OAc$ buffer (pH 7.0), B = ACN, gradient 5% B to 95% in 60 minutes] or by flash chromatography using a DCM:MeOH mobile phase to provide the compound **11** as a brown solid. LC/MS for **11**: LC/MS (m/z): calculated $[M+H]^+$ for $C_{67}H_{81}IN_{10}O_{13}$: 1400.3, observed: 1400.3 g/mol.

**Synthesis of 2,2',2''-(10-((R)-1-(1-((2-(2-((3S,5S)-5-((R)-2-cyano-4,4-difluoropyrrolidine-1-carbonyl)-2-oxopyrrolidin-3-yl)acetyl)isoindolin-4-yl)methyl)-1H-1,2,3-triazol-4-yl)-22-(4-(4-(4-iodophenyl)butanamido)butyl)-21,24-dioxo-2,5,8,11,14,17-hexaoxa-20,23-diazapentacosan-25-yl)-1,4,7,10-tetraazacyclododecane-1,4,7-triyl)triacetic acid (FAP6-IP-DOTA).**

Compound **11** (400 mg, 0.286 mmol) was dissolved in anhydrous DCM (0.5 mL) and diethylamine $(Et)_2NH$ (0.592 mL, 5.72 mmol) then stirred for overnight. Progress of the reaction was monitored via LC/MS. LC/MS (m/z): calculated $[M+H]^+$ for $C_{52}H_{71}F_2IN_{10}O_{10}$, 1178.1; observed: 1178 g/mol. Upon completion of the deprotection, the product was isolated via rotary evaporation, was triturated with EtOAc (2 x10 mL) then

diethyl ether (3 x 10 mL), followed by filtration and dried under vacuum before further use. The deprotected product was dissolved in anhydrous DMF (0.5 mL) and DIPEA (0.150 mL, 0.858 mmol) with DOTA-NHS ester (261 mg, 0.343 mmol) and stirred under inert atmosphere at room temperature for 12 hours. The crude product was purified via RP-HPLC [A = 20 mM $NH_4OAc$ buffer (pH 5.0) and B = $CH_3CN$, solvent gradient 5% B to 35% B in 60 minutes] to yield **FAP6-IP-DOTA**. LC/MS for **FAP6-IP-DOTA**: LC/MS (m/z): calculated $[M+H]^+$ for $C_{68}H_{97}F_2IN_{14}O_{18}$, 1563.4, observed 1563.4 g/mol.

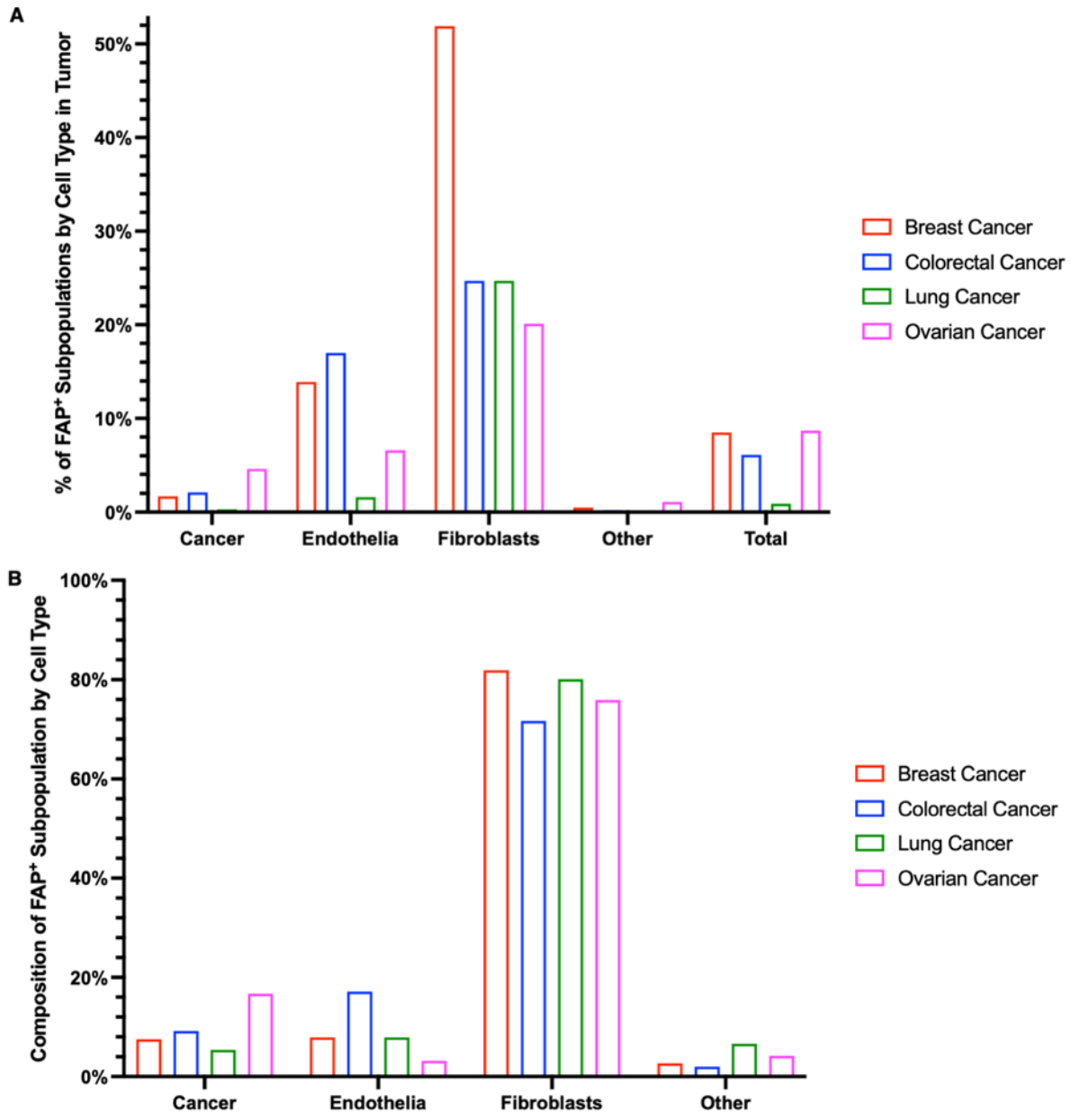


**SUPPLEMENTAL FIGURE 1.** (**A**) Quantification of the subpopulation within each major cell type that overexpresses FAP RNA in the indicated types of human solid tumors. Approximately 2.5% of all cancer cells vs. 30% of all fibroblasts upregulate FAP gene expression in human breast, colorectal, lung and ovarian tumors. (**B**) Identity analysis and relative quantification of the cells within the FAP-overexpressing subpopulation for each type of solid tumor, e.g., a cancer, endothelial or fibroblast cell type. For example, 9.7% of all FAP-overexpressing cells in the indicated solid tumors are cancer cells while 77.4% are fibroblasts. The “Other” category includes myeloid cells, T-cells, B-cells, dendritic cells, and mast cells.

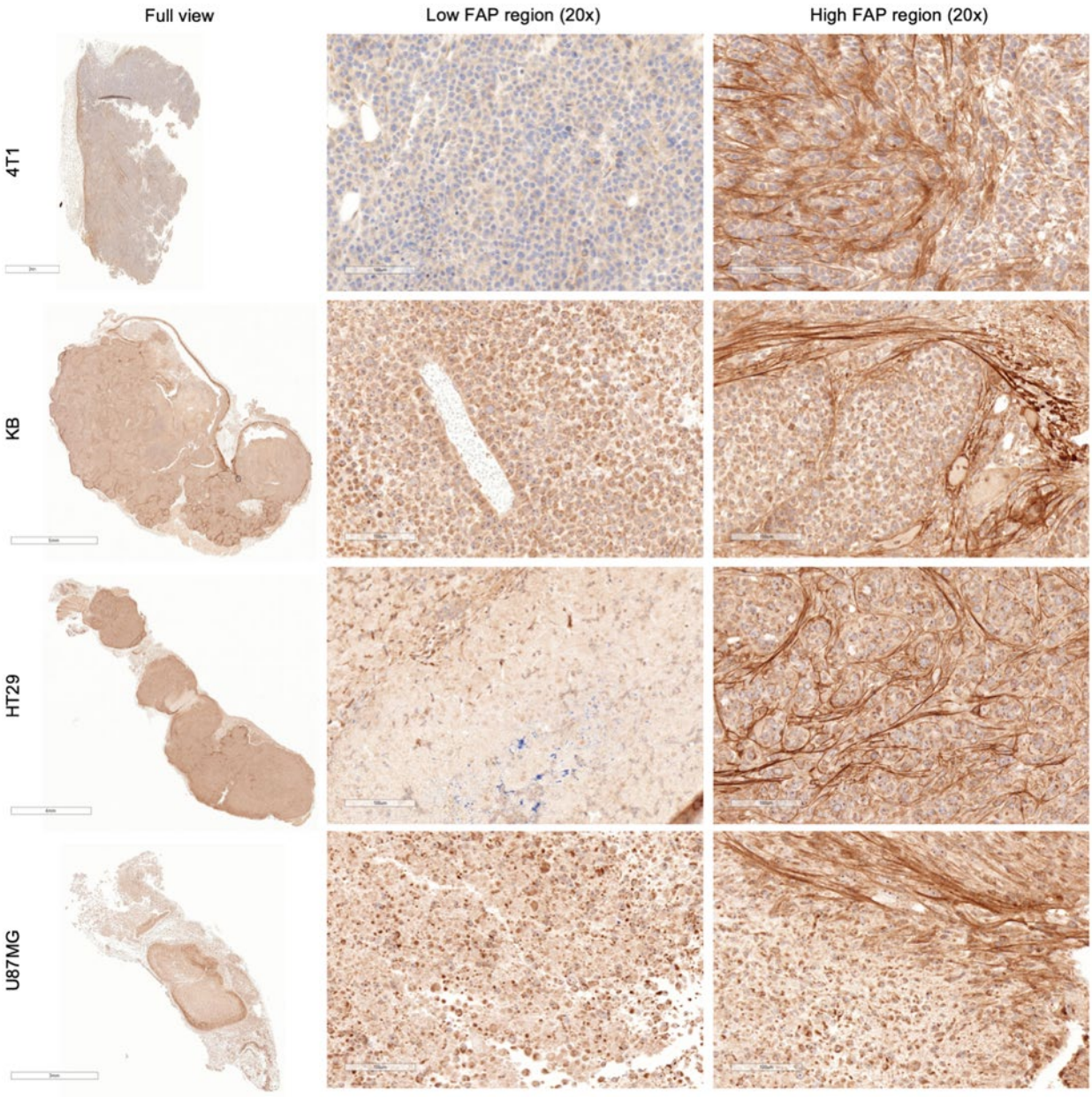


**SUPPLEMENTAL FIGURE 2.** FAP IHC stains of 4T1, KB, HT29, and U87MG tumors. Representative sections of FAP low and high regions within the tumor are also provided at 20x magnification.

**A** FAP6-DOTA LC-MS: $[MH]^+$ = 1368.5 (m/z), calc. = 1367.5


**B** FAP6-IP-DOTA LC-MS: $[MH]^+$ = 1564.5 (m/z), calc. = 1563.5


**SUPPLEMENTAL FIGURE 3.** LC/MS characterization of (**A**) FAP6-DOTA, and (**B**) FAP6-IP-DOTA. LC/MS conditions: gradient = 0.5 min 5% B → 4.5 min 95% B → 5.5 min 95% B → 6.0 min 5% B → 7.0 min 5% B [A = 20 mM pH 7 $NH_4HCO_3$, B = ACN]; flow rate = 0.75 mL/min; DAD = 190–900 nm sweep (λ = 254 nm extracted); ionization energy = 70 eV.

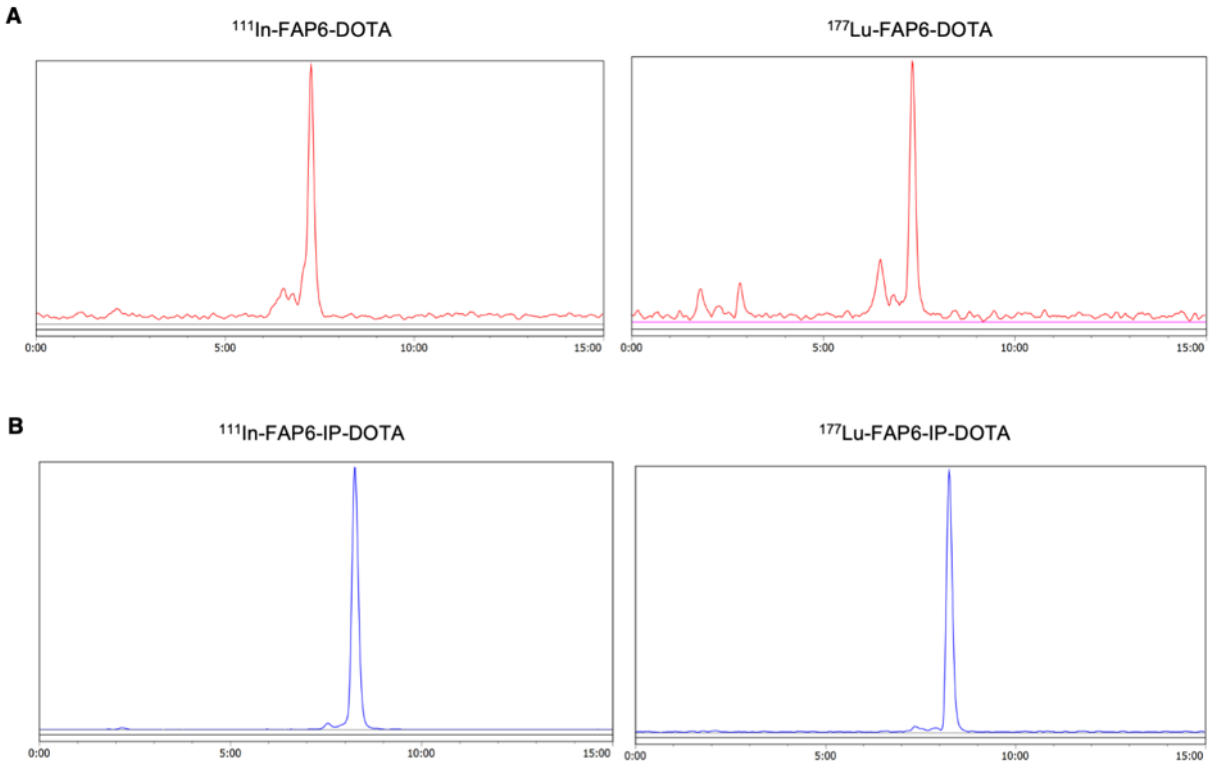


**SUPPLEMENTAL FIGURE 4.** Radiochromatograms of (**A**) $^{111}$In-FAP6-DOTA and $^{177}$Lu-FAP6-DOTA; (**B**) $^{111}$In-FAP6-IP-DOTA and $^{177}$Lu-FAP6-IP-DOTA. Radio-HPLC conditions: gradient = 0.5 min 5% B → 4.5 min 95% B → 10.0 min 95% B → 11.0 min 5% B → 14.0 min 5% B → 15.0 min 5% B [A = 20 mM pH 7 $NH_4HCO_3$, B = ACN]; flow rate = 0.75 mL/min; λ = 254 nm extracted.

A

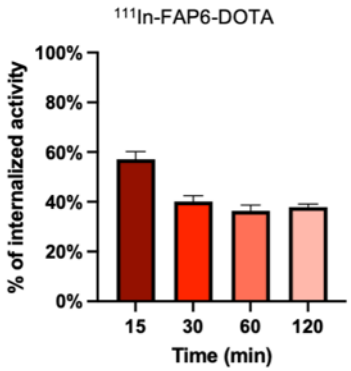


B

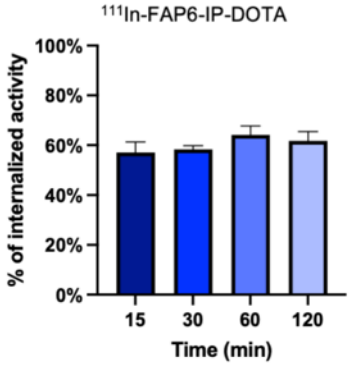


**SUPPLEMENTAL FIGURE 5.** Internalization of (**A**) $^{111}$In-FAP6-DOTA or (**B**) $^{111}$In-FAP6-IP-DOTA in HT1080-hFAP cells.

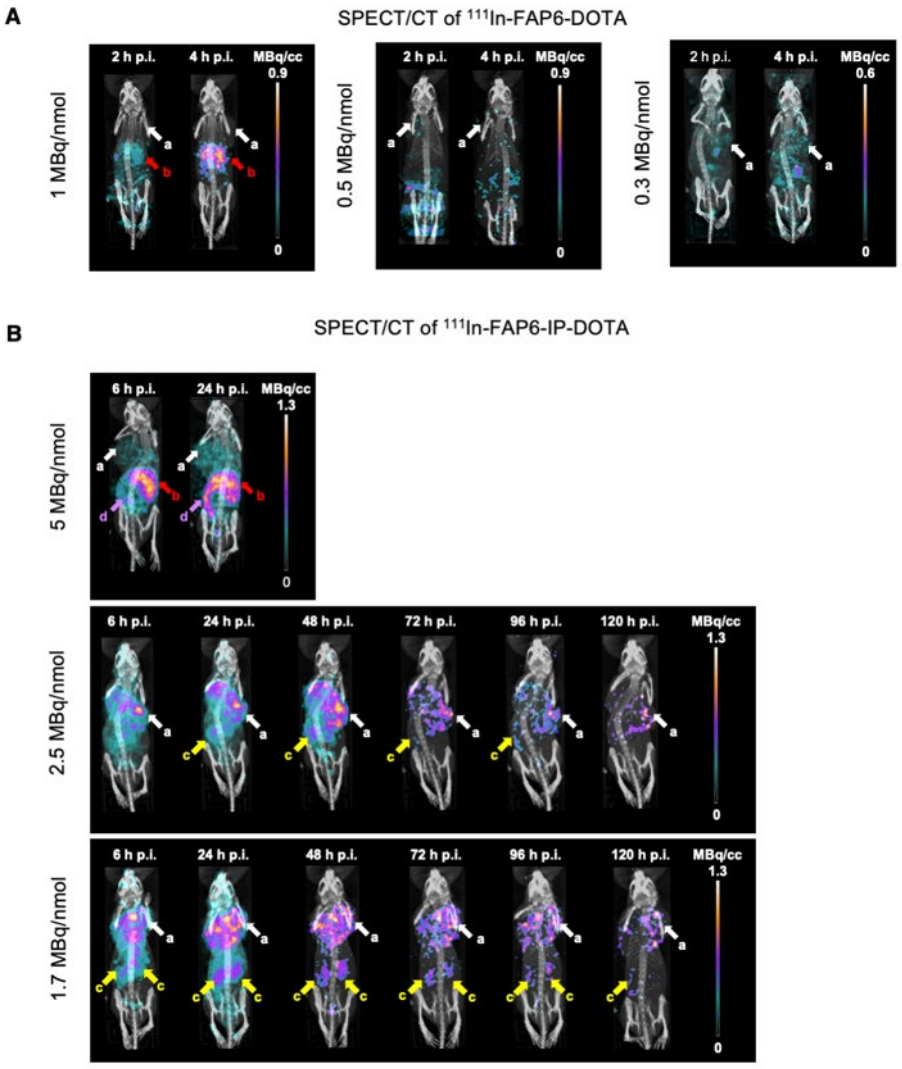


**SUPPLEMENTAL FIGURE 6.** Optimization of the specific activities of (**A**) $^{111}$In-FAP6-DOTA and (**B**) $^{111}$In-FAP6-IP-DOTA conjugates in 4T1 tumors over time as a function of molar amount of FAP6 conjugate injected while maintaining the dose of radioactivity constant (~10 MBq). Arrows: a = 4T1 tumors; b = liver; c = kidneys; d = spleen.

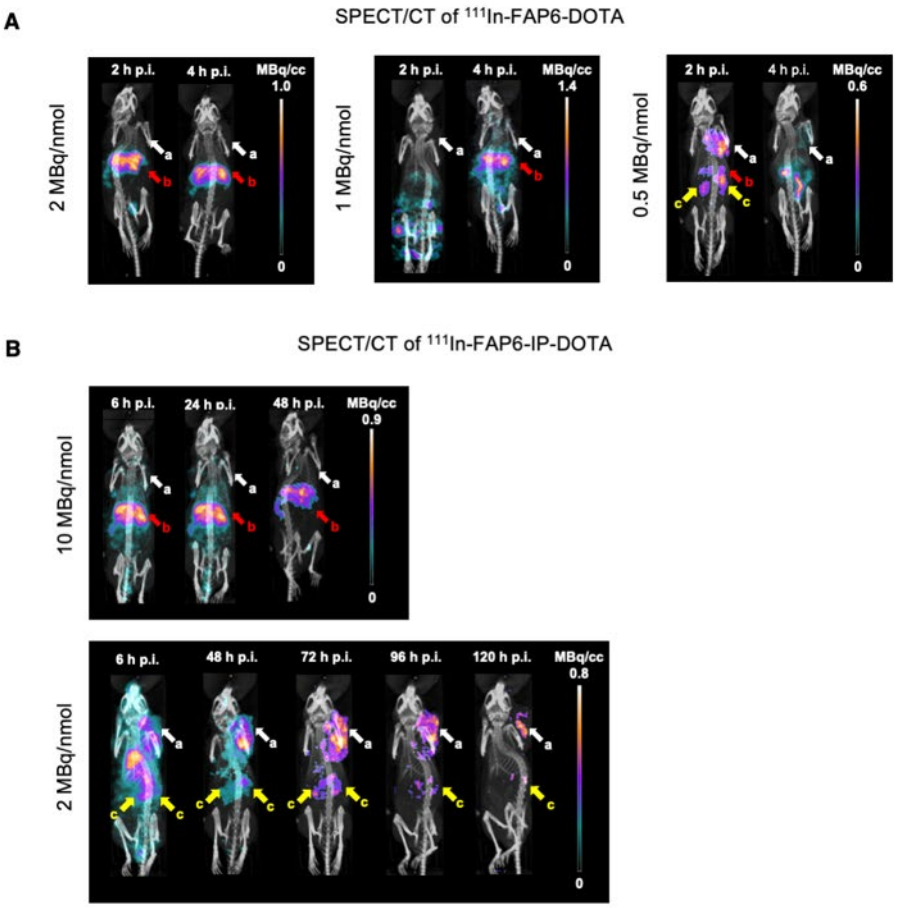


**SUPPLEMENTAL FIGURE 7.** Optimization of the specific activities of (**A**) $^{111}$In-FAP6-DOTA and (**B**) $^{111}$In-FAP6-IP-DOTA in HT29 tumors over time as a function of molar amount of FAP6 conjugate injected while maintaining the dose of radioactivity constant (~10 MBq). Arrows: a = 4T1 tumors; b = liver; c = kidneys.

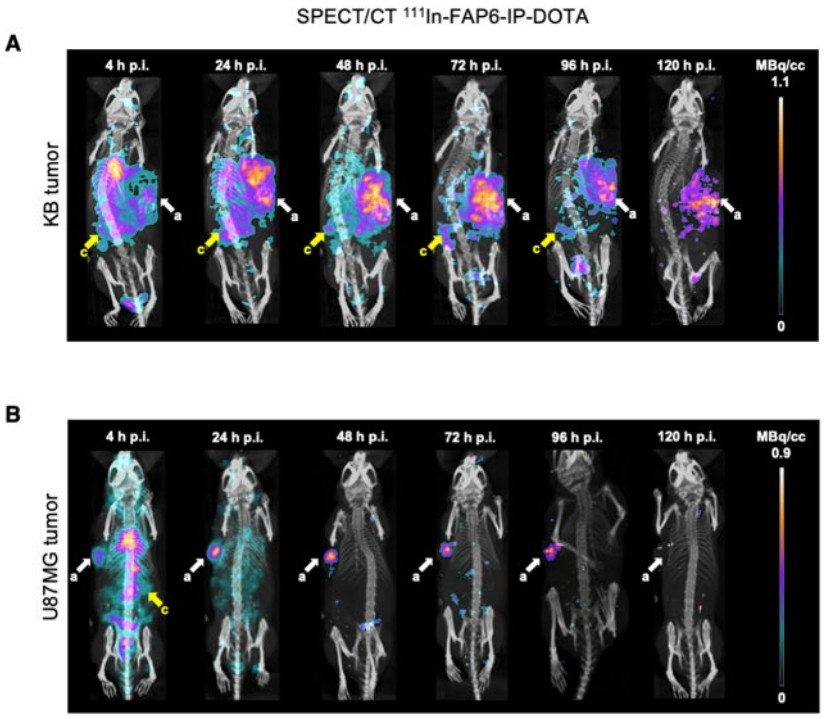


**SUPPLEMENTAL FIGURE 8.** Retention of $^{111}$In-FAP6-IP-DOTA in (**A**) KB and (**B**) U87MG tumors as a function of time after injection. a: 4T1 tumors; b: liver; c: kidneys.

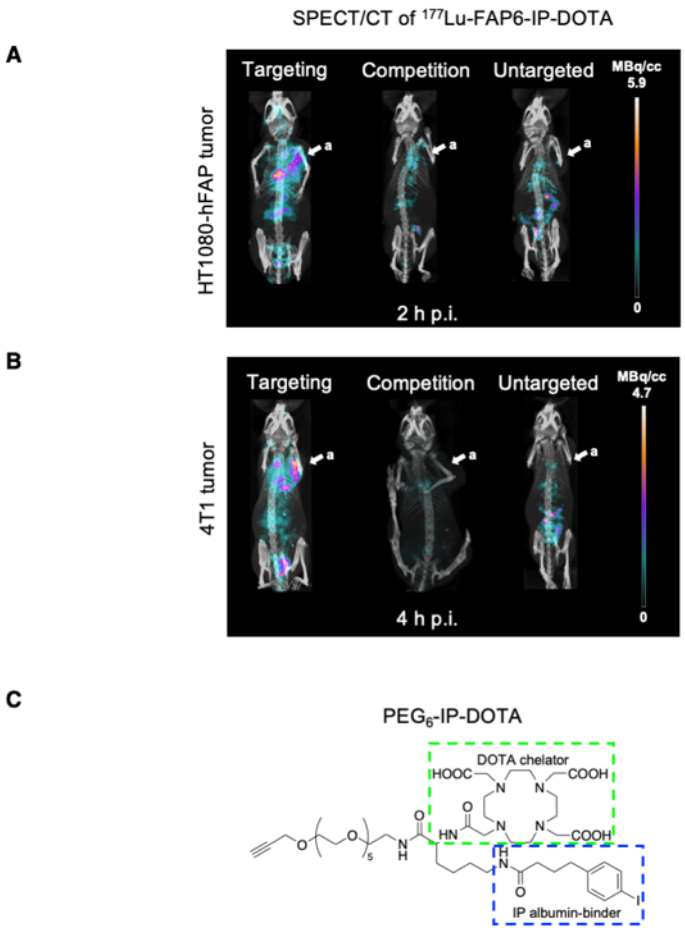


**SUPPLEMENTAL FIGURE 9.** Specificity studies of FAP6-IP-DOTA were conducted with $^{111}$In-FAP6-IP-DOTA alone (targeting), $^{111}$In-FAP6-IP-DOTA + 100x excess of cold compound (competition), or $^{111}$In-PEG$_6$-IP-DOTA (untargeted). SPECT/CT scans were performed under all 3 conditions in (**A**) HT1080-hFAP and (**B**) 4T1 tumors. a: Tumors; b: liver; c: kidneys. (**C**) The molecular structure of PEG$_6$-IP-DOTA is provided, which was synthesized, radiolabeled, and evaluated in a manner analogous to FAP6-IP-DOTA.

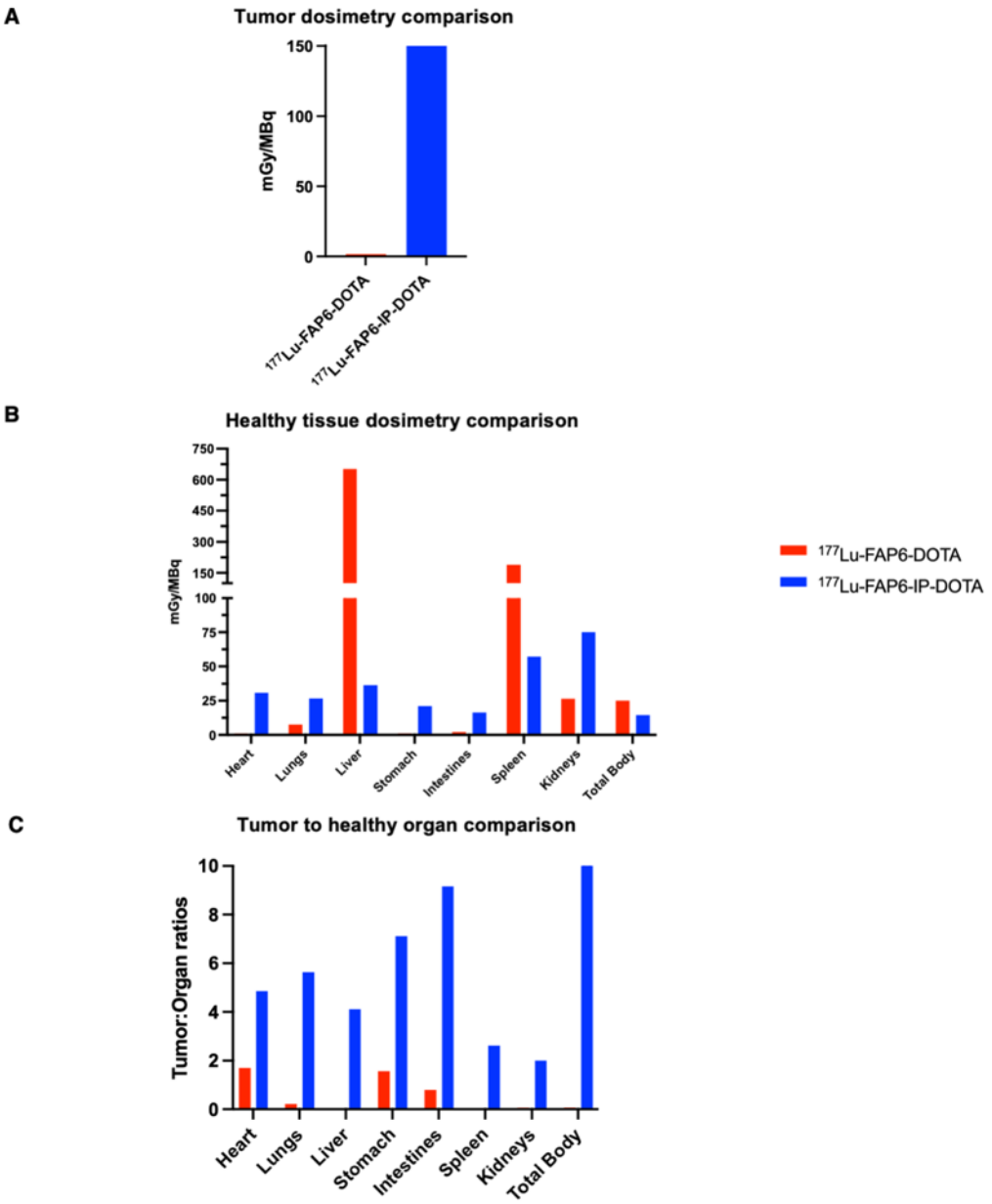


**SUPPLEMENTAL FIGURE 10.** Comparison of radiation dose estimates (mGy/MBq) delivered by $^{177}$Lu-FAP6-DOTA (red bars) and $^{177}$Lu-FAP6-IP-DOTA (blue bars) to (**A**) 4T1 tumors and (**B**) healthy organs as calculated by OLINDA 2.2.3. (**C**) Tumor to healthy organ ratios based on the calculated dosimetries in panels A and B are also provided.

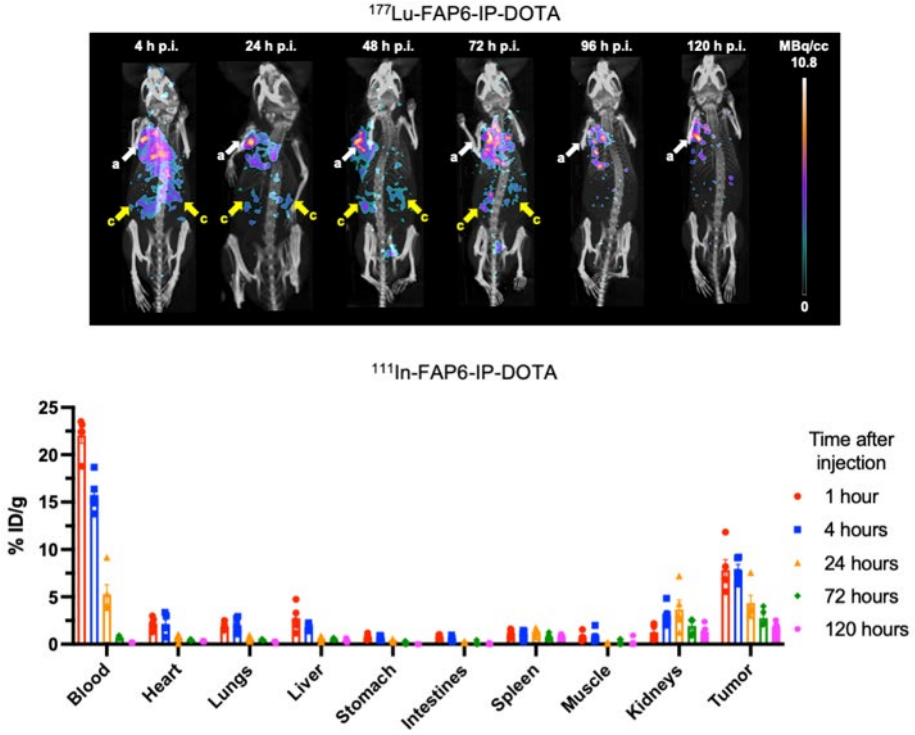


**SUPPLEMENTAL FIGURE 11.** SPECT/CT scans of $^{177}$Lu-FAP6-IP-DOTA and biodistribution analysis of $^{111}$In-FAP6-IP-DOTA in 4T1 tumor-bearing mice as a function of time after injection.

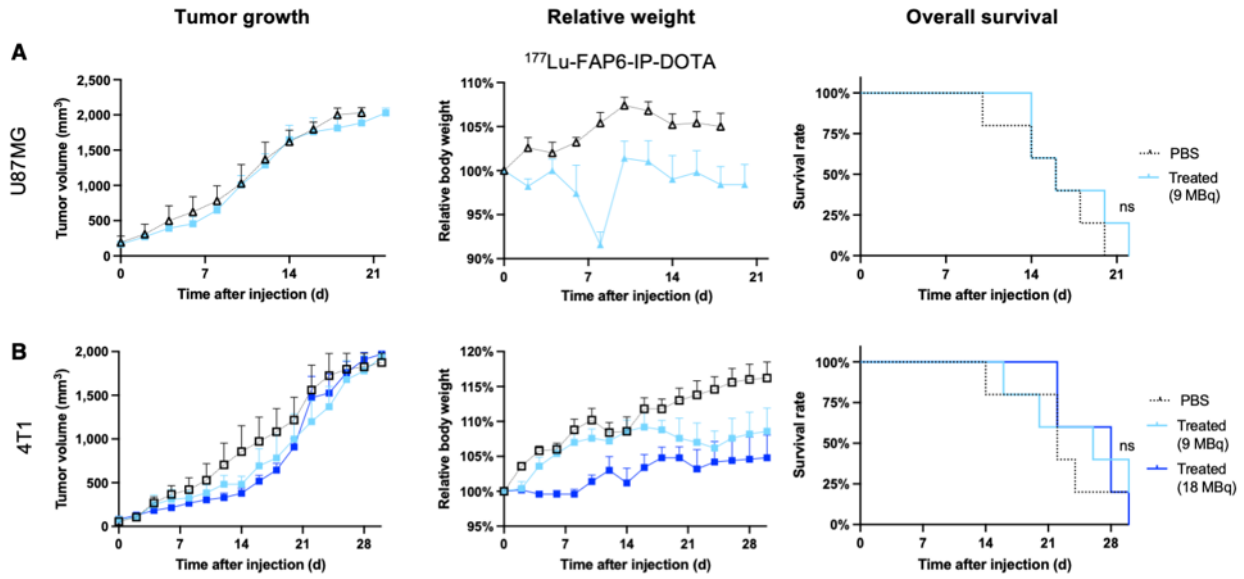


**SUPPLEMENTAL FIGURE 12.** Radioactive doses of $^{177}$Lu-FAP6-IP-DOTA that were not effective for different tumor models are reported here. Briefly, mice bearing (**A**) U87MG (n = 5/group) or (**B**) 4T1 (n = 5/group) tumors received a single injection of $^{177}$Lu-FAP6-IP-DOTA radiolabeled with the indicated amount of activity on day 0.

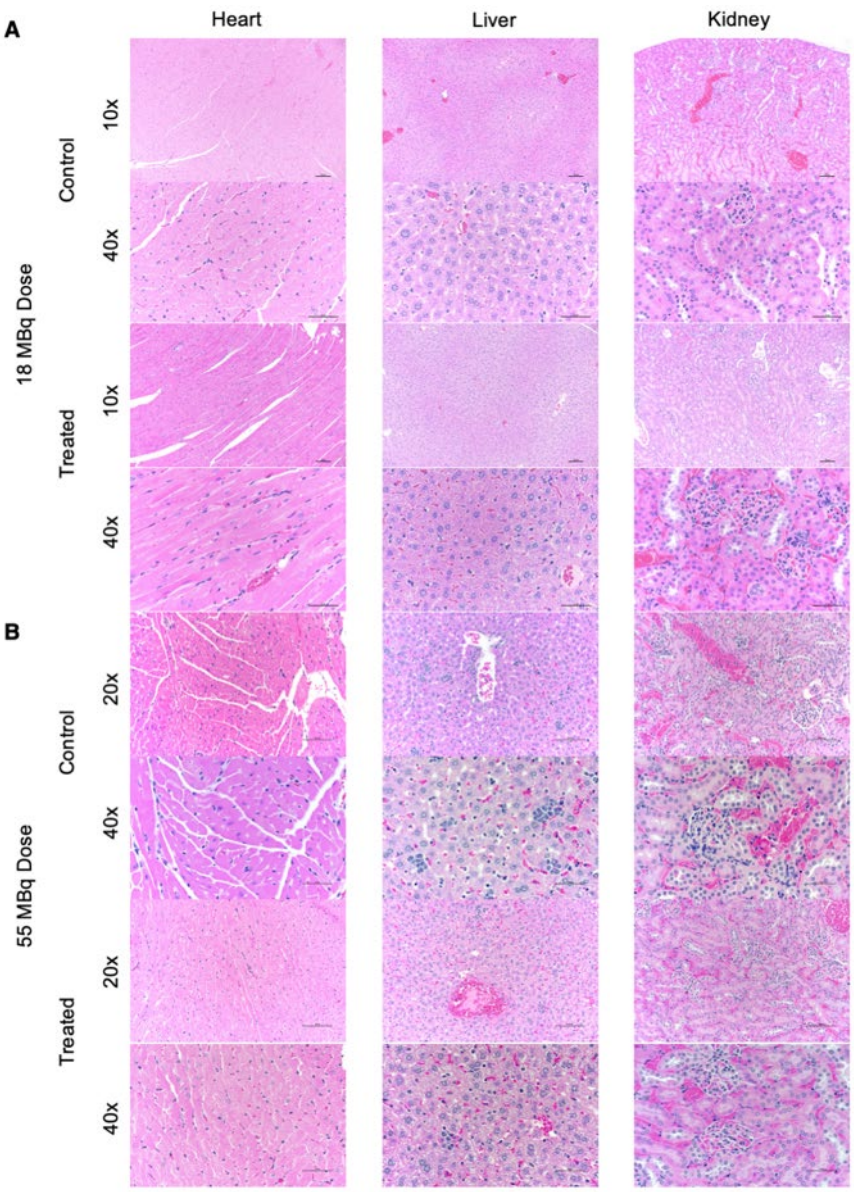


**SUPPLEMENTAL FIGURE 13.** Representative photomicrographs of 4 μm sections of mouse heart, liver, and kidney tissue following radiotherapy treatments of a single dose of $^{177}$Lu-FAP6-IP-DOTA from Figures 5 and 6 [(**A**) 18 MBq in athymic nu/nu mice and (**B**) 55 MBq in Balb/c mice] stained with H&E.

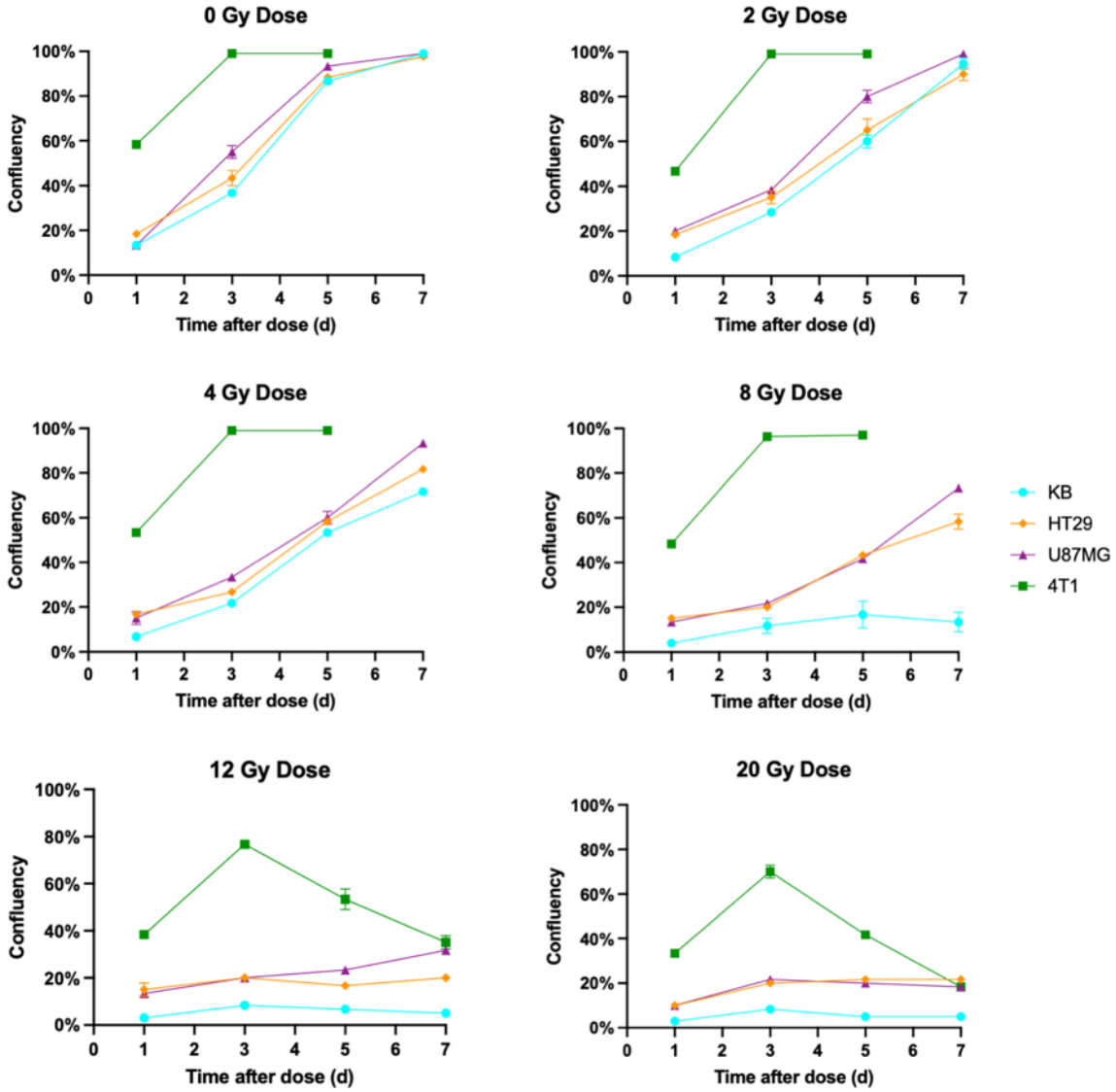


**SUPPLEMENTAL FIGURE 14.** The relative radiosensitivities of KB (●), HT29 (♦), U87MG (▲), and 4T1 (■) tumor cell lines were assessed by irradiation with an external beam at the indicated doses, followed by evaluation of the confluency of the cells every other day.

**SUPPLEMENTAL TABLE 1.** Biodistribution results of $^{177}$Lu-FAP6-DOTA, $^{177}$Lu-FAP6-IP-DOTA, and $^{111}$In-FAP6-IP-DOTA in 4T1 tumors.

| Organs | $^{177}$Lu-FAP6-DOTA in 4T1 tumors %ID/g mean ± SE | | | | |
|---|---|---|---|---|---|
| | 1 hours p.i. | 4 hours p.i. | 24 hours p.i. | 72 hours p.i. | 120 hours p.i. |
| Blood | 0.45 ± 0.10 | 0.64 ± 0.41 | 0.01 ± 0.00 | 0.01 ± 0.00 | 0.01 ± 0.00 |
| Heart | 0.13 ± 0.01 | 0.04 ± 0.01 | 0.02 ± 0.00 | 0.05 ± 0.03 | 0.01 ± 0.00 |
| Lungs | 0.38 ± 0.04 | 0.09 ± 0.02 | 0.07 ± 0.03 | 0.04 ± 0.01 | 0.02 ± 0.01 |
| Liver | 8.99 ± 2.57 | 3.74 ± 2.11 | 6.32 ± 3.00 | 7.73% ± 3.02 | 5.19 ± 1.70 |
| Stomach | 0.02 ± 0.00 | 0.08 ± 0.03 | 0.04 ± 0.03 | 0.01 ± 0.00 | 0.01 ± 0.00 |
| Intestines | 0.14 ± 0.07 | 0.17 ± 0.13 | 0.01 ± 0.00 | 0.00 ± 0.00 | 0.00 ± 0.00 |
| Spleen | 2.62 ± 1.17 | 1.00 ± 0.45 | 1.80 ± 1.03 | 2.92 ± 0.83 | 1.90 ± 0.41 |
| Muscle | 0.02 ± 0.01 | 0.11 ± 0.03 | 0.02 ± 0.01 | 0.00 ± 0.00 | 0.00 ± 0.00 |
| Kidneys | 0.68 ± 0.16 | 0.53 ± 0.18 | 0.31 ± 0.09 | 0.24 ± 0.08 | 0.42 ± 0.11 |
| Tumor | 0.09 ± 0.05 | 0.09 ± 0.03 | 0.03 ± 0.01 | 0.01 ± 0.01 | 0.02 ± 0.01 |
| | $^{177}$Lu-FAP6-IP-DOTA in 4T1 tumors %ID/g mean ± SE | | | | |
| Blood | 50.95 ± 3.97 | 28.13 ± 2.85 | 1.82 ± 0.10 | 0.19 ± 0.02 | 0.08 ± 0.00 |
| Heart | 2.14 ± 0.46 | 1.56 ± 0.19 | 0.41 ± 0.06 | 0.07 ± 0.04 | 0.05 ± 0.01 |
| Lungs | 2.12 ± 0.62 | 0.83 ± 0.21 | 0.71 ± 0.07 | 0.08 ± 0.01 | 0.06 ± 0.00 |
| Liver | 4.43 ± 0.27 | 1.17 ± 0.26 | 0.61 ± 0.08 | 0.13 ± 0.00 | 0.09 ± 0.01 |
| Stomach | 1.81 ± 0.27 | 0.88 ± 0.23 | 0.32 ± 0.06 | 0.04 ± 0.01 | 0.04 ± 0.01 |
| Intestines | 0.94 ± 0.15 | 0.71 ± 0.24 | 0.22 ± 0.03 | 0.05 ± 0.01 | 0.03 ± 0.00 |
| Spleen | 3.21 ± 0.25 | 2.55 ± 0.11 | 0.91 ± 0.15 | 0.32 ± 0.06 | 0.19 ± 0.01 |
| Muscle | 0.78 ± 0.17 | 0.73 ± 0.16 | 0.15 ± 0.02 | 0.04 ± 0.01 | 0.04 ± 0.01 |
| Kidneys | 2.77 ± 0.60 | 2.18 ± 0.58 | 0.88 ± 0.19 | 0.65 ± 0.15 | 0.46 ± 0.04 |
| Tumor | 12.15 ± 1.61 | 11.10 ± 1.89 | 2.16 ± 0.29 | 1.05 ± 0.24 | 0.54 ± 0.04 |
| | $^{111}$In-FAP6-IP-DOTA in 4T1 tumors %ID/g mean ± SE | | | | |
| Blood | 22.06 ± 0.84 | 15.77 ± 0.84 | 5.28 ± 1.01 | 0.70 ± 0.05 | 0.18 ± 0.01 |
| Heart | 2.19 ± 0.30 | 2.12 ± 0.48 | 0.62 ± 0.21 | 0.44 ± 0.02 | 0.31 ± 0.03 |
| Lungs | 1.87 ± 0.19 | 2.00 ± 0.37 | 0.56 ± 0.13 | 0.46 ± 0.02 | 0.23 ± 0.05 |
| Liver | 2.73 ± 0.61 | 1.82 ± 0.15 | 0.55 ± 0.13 | 0.54 ± 0.03 | 0.41 ± 0.07 |
| Stomach | 0.77 ± 0.12 | 0.65 ± 0.11 | 0.40 ± 0.06 | 0.15 ± 0.06 | 0.01 ± 0.01 |
| Intestines | 0.80 ± 0.10 | 0.56 ± 0.11 | 0.23 ± 0.04 | 0.12 ± 0.08 | 0.03 ± 0.03 |
| Spleen | 1.20 ± 0.18 | 1.04 ± 0.20 | 1.33 ± 0.18 | 0.79 ± 0.13 | 0.85 ± .0.08 |
| Muscle | 0.77 ± 0.21 | 0.85 ± 0.29 | 0.13 ± 0.02 | 0.25 ± 0.11 | 0.20 ± 0.18 |
| Kidneys | 1.26 ± 0.31 | 3.07 ± 0.49 | 3.68 ± 1.01 | 1.93 ± 0.38 | 1.31 ± 0.33 |
| Tumor | 7.85 ± 1.08 | 7.86 ± 0.57 | 4.36 ± 0.81 | 2.77 ± 0.40 | 1.87 ± 0.22 |

**SUPPLEMENTAL TABLE 2.** Summarized histopathology of necropsy tissues post treatment.

| Dose | Group | Organ | Total sections examined | | | | | | Diagnostic lesions | | | | | |
|---|---|---|---|---|---|---|---|---|---|---|---|---|---|---|
| 18 MBq | *Control (n = 2)* | *Liver* | 8 | | | | | | 0 | | | | | |
| | | *Kidneys* | 16 | | | | | | 0 | | | | | |
| | | *Myocardium* | 8 | | | | | | 0 | | | | | |
| | *Treated (n = 7)* | *Liver* | 38 | | | | | | 0 | | | | | |
| | | *Kidneys* | 56 | | | | | | 0 | | | | | |
| | | *Myocardium* | 28 | | | | | | 0 | | | | | |
| | | | *Time after injection (d)* | | | | | | *Time after injection (d)* | | | | | |
| | | | *1* | *3* | *7* | *14* | *21* | *Total* | *1* | *3* | *7* | *14* | *21* | *Total* |
| 55 MBq | *Control (n = 5)* | *Liver* | 2 | 1 | 1 | 1 | 1 | 7 | 0 | 0 | 1 | 1 | 1 | 3 |
| | | *Kidneys* | 4 | 4 | 4 | 4 | 4 | 20 | 0 | 0 | 0 | 0 | 0 | 0 |
| | | *Myocardium* | 2 | 2 | 2 | 2 | 2 | 10 | 1 | 0 | 1 | 1 | 0 | 3 |
| | *Treated (n = 15)* | *Liver* | 5 | 3 | 3 | 3 | 3 | 17 | 0 | 0 | 0 | 0 | 2 | 2 |
| | | *Kidneys* | 12 | 12 | 12 | 12 | 12 | 60 | 0 | 2 | 0 | 0 | 0 | 2 |
| | | *Myocardium* | 6 | 6 | 6 | 6 | 6 | 30 | 0 | 0 | 0 | 0 | 1 | 1 |

**References**

**1.** Qian J, Olbrecht S, Boeckx B, et al. A pan-cancer blueprint of the heterogeneous tumor microenvironment revealed by single-cell profiling. *Cell Res.* 2020;30:745-762.

**2.** SCope tutorial: Pan-cancer TME blueprint. August 3, 2021; http://scope.lambrechtslab.org/#/a0f9b96f-e2d9-4156-9899-993e37a62c03/Breast.loom/tutorial. Accessed February 15, 2022.

**3.** Mukkamala R, Lindeman SD, Kragness KA, et al. Design and characterization of fibroblast activation protein targeted pan-cancer imaging agent for fluorescence-guided surgery of solid tumors. *J Mater Chem B.* 2022;10:2038-2046.

**4.** Tsai T-Y, Yeh T-K, Chen X, et al. Substituted 4-carboxymethylpyroglutamic acid diamides as potent and selective inhibitors of fibroblast activation protein. *J Med Chem.* 2010;53:6572-6583.